Article:
Jimenez-Arias, JL, Mata, MP, Corzo, A et al. (8 more authors) (2016) A multiproxy study distinguishes environmental change from diagenetic alteration in the recent sedimentary record of the inner Cadiz Bay (SW Spain). The Holocene, 26 (9). pp. 1355-1370. ISSN 0959-6836

https://doi.org/10.1177/0959683616640046

A multiproxy study distinguishes environmental change from diagenetic alteration in the recent sedimentary record of the inner Cadiz Bay (SW Spain)

Juan L. Jiménez-Arias[1,*], M. Pilar Mata[2;a], Alfonso Corzo[1], Simon W. Poulton[3], Christian März[4], Angel Sánchez-Bellón[2], Javier Martínez-López[2], Melquiades Casas-Ruiz[5], Emilio García-Robledo[1;b], Julio Bohórquez[1], Sokratis Papaspyrou[1;6;c]

1 Department of Biology, Faculty of Marine and Environmental Science, University of Cadiz, Pol. Rio San Pedro s/n, 11510 Puerto Real, Spain

2 Department of Earth Sciences, Faculty of Marine and Environmental Sciences, University of Cadiz, Pol. Rio San Pedro s/n, 11510 Puerto Real, Spain

3 School of Earth and Environment, University of Leeds, Leeds LS2 9JT, UK

4 School of Civil Engineering and Geosciences, Newcastle University, Newcastle upon Tyne NE1 7RU, UK

5 Department of Applied Physics, Faculty of Marine and Environmental Sciences, University of Cadiz, Pol. Rio San Pedro s/n, 11510 Puerto Real, Spain

6 Instituto de Ciencias Marinas de Andalucía (ICMAN-CSIC), Pol. Río San Pedro s/n, 11510 Puerto Real, Spain

Present addresses:
a Instituto Geológico y Minero de España, C/ La Calera, 1, 28760 Tres Cantos, Madrid, Spain
b Section for Microbiology, Department of Bioscience, Aarhus University, Ny Munkegade 114, DK-8000 Aarhus C, Denmark
c Departamento de Biomedicina, Biotecnología y Salud Publica, Universidad de Cádiz, University of Cadiz, Pol. Rio San Pedro s/n, 11510 Puerto Real, Spain

*Corresponding author:
Tel.: +34 956 016177
Fax: +34 956 016019
Email address: juan.jimenezarias@uca.es (Juan Luis Jiménez Arias)

Abstract

In this study we reconstruct the recent environmental evolution of the inner Cadiz Bay using sedimentary records reaching back as far as 1700 AD. We report lithological descriptions of the sediments, and extensive mineralogical and geochemical analyses. An extraction technique that identifies different Fe phases provides an assessment of diagenetic alteration, which allows an estimation of the original organic matter inputs to the inner Cadiz Bay. Downcore variations in C_{org}/N ratios, $\delta^{13}C_{org}$, and $\delta^{15}N$ are related to changes in organic matter sources and the trophic state of the water column. The downcore records of selected trace metals (e.g., Pb, Zn, Cu) are interpreted to reflect changes in heavy metal pollution in the bay, while records of other elements (e.g., Mn, P) are likely overprinted by diagenetic alteration. Major environmental shifts took place during the 20^{th} century, when the population around Cadiz Bay increased exponentially. Increases in sediment accumulation rates, organic matter inputs, and heavy metal contents, in parallel with increases in $\delta^{13}C_{org}$ and $\delta^{15}N$ over this period, are interpreted as direct effects of the increasing anthropogenic influence in the area. The results of this study suggest that multi-proxy approaches and detailed consideration of diagenetic overprinting are required to reconstruct past environmental conditions from coastal sediments.

Key words

^{210}Pb dating; Cadiz Bay; coastal sediments; early Holocene; iron speciation; multiproxy, organic matter sources; pollution; sedimentation rates; Spain; stable isotopes; x-ray fluorescence core scanner

Introduction

Sedimentary records are valuable environmental archives, allowing reconstruction of ecosystem development over time. Fine-grained sediments from marine basins and sedimentary rocks are typically used to study climate and oceanographic changes in the geologic past (Sageman & Lyons, 2005 and references therein). In contrast, paleoecological studies more commonly use lacustrine (Giralt et al., 2011; Lami et al., 2010; Martín-Puertas et al., 2009) and coastal sediment records (Covelli et al., 2006; Di Leonardo et al., 2012; Lepland et al., 2010), which allow environmental changes to be studied on decadal to sub-decadal time scales. The high temporal resolution of such sediments allows natural changes to be distinguished from those produced by anthropogenic influence, e.g. eutrophication, coastal hypoxia, or metal contamination (Church et al., 2006; Ellegaard et al., 2006; Zimmerman and Canuel, 2000). However, historical paleoecological reconstructions are frequently applied to recent sediments that still contain significant amounts of potentially degradable organic matter. Under these conditions, post-depositional processes related to organic matter remineralization often alter primary geochemical signals preserved in the sediment (Chen et al., 2008; Spencer et al., 2003; Tribovillard et al., 2006). Elements such as C, P, N, and S, along with various metals, can be remobilized within the sediment column, potentially making their sedimentary records unreliable for paleoenvironmental reconstructions. Hence,

20 complementary studies of early diagenetic processes and their effects are required in
21 such sediments.
22 Coastal sediments are considered good inventories of historical contamination
23 from both the hinterland and the coast (Ridgway and Shimmield, 2002). However, these
24 areas are frequently affected by artificial reworking (e.g., shell fishing, dredging,
25 harbour operations) that can create hiatuses in sedimentary records. The identification of
26 such discontinuities requires specific geochemical techniques in addition to
27 mineralogical and textural analyses (Lepland et al., 2010; Ridgway et al., 2000). In fact,
28 the diagenetic overprint caused as a result of these discontinuities can be even more
29 pronounced than that produced by steady-state early diagenetic processes (Deflandre et
30 al., 2002; Mucci and Edenborn, 1992; Mucci et al., 2003). The recognition of
31 secondary diagenetic alteration is crucial for a robust environmental interpretation.
32 Cadiz Bay (SW Spain), with a population of almost 700,000 people in its direct
33 vicinity, has been an important industrial location for many years (e.g. shipbuilding,
34 offshore structure, and aerospace components manufacture). Eutrophication levels
35 (Establier et al., 1990; Gomez-Parra and Forja, 1992) and heavy metal contamination
36 (Ligero et al., 2002) increased in Cadiz Bay over the last few decades of the 20th
37 century. However, in recent years, water column and surface sediment pollution has
38 been reduced, following the regulation of sewage discharges into the coastal
39 environment. Nowadays, the sediments and waters are considered moderately

40 contaminated (Carrasco et al., 2003). However, there is a lack of information on the
41 evolution of the trophic state of the bay over time, and little is known about the
42 development of industrial contamination before 1900. Hence, the evaluation of
43 sedimentary records from Cádiz Bay can be used to provide natural baseline conditions
44 and to determine the effects of anthropogenic activity on the area.
45 The motivation for this study is to analyse the sub-recent environmental evolution
46 of the inner Cadiz Bay using sedimentary records reaching back as far as 1700 AD. The
47 analytical strategy includes the examination of lithofacies and mineralogical
48 composition, geochemical analyses, and radiometric dating techniques. Sedimentary
49 profiles are interpreted within the geological context of Cadiz Bay and its sedimentary
50 dynamics. Special attention is paid to post-depositional alteration, utilizing a sequential
51 iron extraction procedure and other geochemical analyses in parallel. The multi-proxy
52 study presented here allows us to reconstruct major environmental changes that took
53 place in the inner Cadiz Bay over the last few centuries, and to determine the
54 environmental conditions of the pre-industrial period. In particular, our methodological
55 approach enables environmental variations to be differentiated from those induced by
56 diagenetic processes.
57

58 **2. Material and methods**

59 *2.1. The study Area*

60 The Bay of Cadiz, located in the southwest of Spain (36º30'N; 6º10'W; Figure 1) [insert
61 Figure 1.], is defined by a bay or outer bay in its northern part, an island-barrier-lagoon
62 or inner bay system in its southern part, and marshes and tidal planes in its western and
63 eastern parts (Achab, 2011; Muñoz Perez and Sánchez de LaMadrid Rey, 1994). The
64 outer bay (covering 118 km^2), which directly connects to the Atlantic Ocean, is strongly
65 affected by storms, waves, and littoral currents, and its seabed is predominantly sandy.
66 The inner bay (covering 34 km^2) is more sheltered from erosive action, and is
67 characterized by shallow waters (80% of the area with <1 m water depth) and muddy
68 sediments. The marshes and tidal planes (covering 227 km^2) are drained by a network of
69 tidal channels linking the distal zones of the inner bay with the marine environment.
70 The Sancti Petri creek connects the inner bay with the Atlantic Ocean, while the Rio
71 San Pedro creek is a former tributary of Guadalete River that today only acts as a tidal
72 channel.

73 The marshes surrounding the inner bay are dominantly colonised by halophyte
74 plants, whereas the vegetation in the tidal planes shows a vertical zonation in relation to
75 tide height (Morris et al., 2009; Muñoz Perez and Sánchez de LaMadrid Rey, 1994).
76 *Spartina maritima* (a cordgrass) grows in the upper part of the tidal plane, while
77 seagrasses such as *Zostera noltii*, *Cymodocea nodosa* and *Zostera marina* inhabit the
78 lower part. The middle part of the tidal plane has no vegetation although it is inhabited
79 by diatom-dominated microphytobenthic communities. In addition, this zone of bare

80 sediment is covered seasonally by tubular *Ulva spp*, a green macroalga that forms dense
81 blooms throughout the inner bay (Corzo et al., 2009). The subtidal areas of the inner
82 Cadiz Bay are inhabited almost entirely by *Caulerpa prolifera*, a rooted macroalga that
83 forms extensive meadows.
84 The main sediment sources to the inner Cadiz Bay are the Guadalete, Salado and
85 Iro Rivers (Gutiérrez-Mas et al., 1997). In addition, North Atlantic Surface Water
86 (NASW) and littoral currents are considered to be responsible for carrying fine sediment
87 from the Guadalquivir River into the bay (Gutiérrez-Mas et al., 2006). The tidal regime
88 is mesotidal with a semi-diurnal cycle. The tidal currents are responsible for fine
89 sediment dispersal into Cadiz Bay, although wind- and wave-driven currents are also
90 important factors in the sedimentary dynamics (Achab, 2011; Gutiérrez-Mas et al.,
91 2003).
92
93 *2.2. Sample collection*
94 Sediment cores (84-107 cm length, 5.6 cm diameter) were collected at three sites in the
95 inner Cadiz Bay (Figure 1) in September 2009 and April 2011, using a modified
96 UWITEC-core sampler (Table 1). In 2009, one core was recovered at each station (core
97 1MB09, core 2MB09, and core 3MB09). The cores were split lengthwise,
98 photographed, and described sedimentologically. One split half was capped and
99 preserved at 4ºC until further analysis by X-Ray Fluorescence (XRF); the other half was

100 **Table 1.** Summary of the geographical coordinates, sampling dates, and water column depths for sampled cores

101

Core	**1MB09**	**11MB11**	**12MB11**	**13MB11**	**2MB09**	**21MB11**	**22MB11**	**23MB11**	**3MB09**
Position	36º 31.140 N 06º 11.400 W	36º 30.540 N 06º 12.030 W	36º 30.540 N 06º 12.040 W	36º 30.540 N 06º 12.030 W	36º 29.380 N 06º 14.040 W	36º 30.126 N 06º 14.073 W	36º 30.126 N 06º 14.073 W	36º 30.126 N 06º 14.073 W	36º 29.020 N 06º 14.320 W
Sampling	September 2009	April 2011	April 2011	April 2011	September 2009	April 2011	April 2011	April 2011	September 2009
Length	106 cm	100 cm	107 cm	89 cm	98 cm	100 cm	103 cm	84 cm	107 cm
Water column	0.9 m	0.5-1 m	0.5-1 m	0.5-1 m	2.4 m	0.5-1 m	0.5-1 m	0.5-1 m	2.7 m
Zone	Z 1	Z 1	Z 1	Z 1	Z 2	Z 2	Z 2	Z 2	Z 3
Analyses	Sedimentology XRD XRF	XRF	Sequential Fe/S extractions ICP-OES Total C-N Stable isotopes	Dating-Pb^{210}	Sedimentology XRD XRF	XRF	Sequential Fe/S extractions ICP-OES Total C-N Stable isotopes	Dating-Pb^{210}	Sedimentology XRD XRF

102

103

104

105 sliced in 1 cm resolution down to 20 cm sediment depth, and in 2 cm resolution at
106 greater depths. Each sediment slice was dried at room temperature and ground in an
107 agate mortar for mineralogical analysis, discarding shells and other larger fragments of
108 calcium carbonate during handling. In 2011, three sediment cores were taken from
109 sampling site 1 and sampling site 2, respectively. One core of each station was kept at 4º
110 C for XRF analysis (core 11MB11, core 21MB11); the second core was immediately
111 processed under an N_2 atmosphere (see below) and used for further geochemical
112 analysis of redox sensitive elements (core 12MB11, core 22MB11); the third core was
113 frozen at -20ºC and utilized for ^{210}Pb dating (core 13MB11, core 23MB11).
114 Cores 12MB11 and 22MB11 were sliced every 2 cm for the first 60 cm depth and
115 then every 4 cm under a N_2 atmosphere. The sediment samples were freeze-dried and
116 kept at -20ºC. One subsample was used for partitioning of iron and total element
117 contents in the solid phase; the second was used for bulk analysis of organic carbon,
118 carbonate and nitrogen; the third was utilized for stable isotope analysis of organic
119 carbon and total nitrogen. Wet bulk density, dry bulk density, and sediment porosity
120 were calculated from the loss of weight during freeze-drying of each slice (see
121 supplementary material).
122
123 *2.3. Sedimentary characteristics and mineralogical analysis*

124 Features considered in the sedimentary description included texture, colour,
125 sedimentary structures, bioclast content, and grain size. The colour was determined on
126 wet sediment, using Munsell Soil Color Charts. Mineralogical analysis was performed
127 with a Bruker D8-Advanced Diffractometer using the crystalline powder technique.
128 Diffractograms were obtained with scans from 2º to 60º 2θ, radiation Cu-Kα =
129 1.5405Aº, step size = 0.04º 2θ and time = 1 s. Mineralogical composition was
130 determined by comparing the intensities of each mineral phase with the EVA© software
131 database references. The semi-quantitative analysis of different mineral phases followed
132 the Reference Intensity Ratio (RIR) values method (Chung, 1974). Clay minerals were
133 taken into account in the mineralogical analysis and quantified in total by the peak
134 intensity of 20º 2θ. The following RIR values were chosen for each mineral phase:
135 gypsum (1.8), clay minerals (0.1), goethite (2.7), rutile (1), barite (2.8), aragonite (1),
136 quartz (3.1), orthoclase (0.8), albite (0.7), calcite (1), ankerite (2.8), dolomite (2.7),
137 apatite (1), halite (4.7), pyrite (0.9), and hematite (3).
138
139 *2.4. XRF core scanning*
140 Energy-dispersive XRF core scanner measurements were carried out directly on the
141 split core surface with an Avaatech XRF core scanner (Department of Marine
142 Geosciences, University of Barcelona) and semi-quantitative element intensity records
143 from Al through Ba were obtained. The XRF scanner was run at 1 cm depth resolution

144 with a scanning time of 10, 25 and 30 s for 10, 30 and 50 kV, respectively. Cores were
145 imaged with a digital Color Line Scan Camera, using visible light with a resolution of
146 140 ppcm (350 dpi). Element profiles generated by XRF core scanning were used to
147 correlate between sediment cores taken at the same locations during the two different
148 cruises.
149
150 *2.5. C-N analysis*
151 Total carbon (TC) and total nitrogen (TN) contents were determined by combustion of
152 untreated samples using an elemental analyzer (LECO CHNS 932). The precision of
153 analysis for the apparatus used was 0.3%. Inorganic carbon (C_{inorg}) was analyzed on
154 sample splits combusted at 550ºC for 5 h before elemental analysis, and was
155 recalculated to the equivalent amount of $CaCO_3$. Organic carbon (C_{org}) was calculated
156 as the difference between TC and C_{inorg}. We report C_{org}/N as molar ratios.
157
158 *2.6. Stable isotope analyses*
159 Isotopic analysis of C_{org} and TN was performed on an elemental analyzer
160 (FlashEA1112, ThermoFinnigan) attached to a stable isotope ratio mass spectrometer
161 (Deltaplus, ThermoFinnigan). Results for C and N isotope compositions are reported in
162 delta notation (‰) relative to Vienna PeeDee Belemnite (VPDB) and atmospheric air,

163 respectively. The precision of analysis for the equipment used is 0.15‰. The $\delta^{13}C_{org}$
164 isotope analyses were performed on samples decarbonated with 2 N HCl.
165
166 *2.7. Major and trace element analysis*
167 Major and trace elements in the sediment were extracted with an HF-$HClO_4$-HNO_3
168 solution. The digestion was performed in Teflon crucibles with approximately 50 mg of
169 combusted samples (550ºC, overnight). Then, H_3BO_3 (50 g L^{-1}) was added to the
170 samples to solubilise Al. Total Al, Mn, P, Cd, Cr, Cu, Ni, Pb, V, and Zn were analysed
171 by Inductively Coupled Plasma Optical Emission Spectrometry (ICP-OES, Varian
172 Vista-MPX). The relative standard deviation (RSD) for ICP-OES analysis was below
173 10% for all elements. Total iron was measured by Atomic Absorption Spectroscopy
174 (AAS, SpectrAA Varian 400).
175
176 *2.8. Sequential iron extractions*
177 Sedimentary Fe speciation was determined using a modified version of the sequential
178 extraction technique of Poulton and Canfield (2005). Approximately 100 mg of freeze-
179 dried and homogenised sediment were subjected to a three step extraction procedure
180 using 10 mL of extractant in each step. First, samples were subjected to a 0.5 N HCl
181 extraction for 1 h to release poorly crystalline hydrous ferric oxides ($Fe(III)_{HFO}$) plus
182 any Fe(II) associated with particle surfaces or FeS ($Fe(II)_{red}$) (see Goldberg et al. 2012;

183 Zegeye et al. 2012). Second, crystalline ferric oxyhydroxides, such as goethite and
184 hematite (Fe_{ox}), were extracted using a freshly prepared Na-dithionite solution (50 g/L
185 buffered to pH 4.8 with 0.2 M Na-citrate and 0.35 M acetic acid) for 2 h. Finally,
186 magnetite (Fe_{mag}) was determined via a 6 h NH_4^+-oxalate (0.2 M NH_4^+-oxalate and 0.17
187 M oxalic acid) extraction. Fe(II) extracted in the first extraction step was analysed using
188 the ferrozine assay (Stookey 1970), and total Fe in each extract was determined via
189 AAS, with a precision better than 3% for all steps. Iron bound to sulphides (Fe_{sulf}),
190 including pyrite (FeS_2) and acid-volatile sulphide (AVS), was determined via the two
191 step distillation technique of Canfield et al. (1986) in sample splits (approximately 500
192 mg freeze-dried sediment). First, AVS was extracted with hot 6 N HCl; then, chromium
193 reducible sulphide (CRS; mostly FeS_2) was extracted with hot 0.1 M $CrCl_2$. The H_2S
194 released during the distillation was trapped in a 1 M $AgNO_3$ solution. The precipitated
195 Ag_2S was retained on a pre-weighed nitrocellulose filter and weighed. Finally, Fe_{sulf}
196 was calculated by converting the Ag_2S weight to FeS and FeS_2 equivalents. The sum of
197 $Fe(III)_{HFO}$, $Fe(II)_{red}$, Fe_{ox}, Fe_{mag} and Fe_{sulf} forms the highly reactive Fe pool (Fe_{HR})
198 (Poulton et al., 2004a, 2004b).
199
200 *2.9. Dating of sediments and calculation of sedimentation rates*
201 Sediment cores were sliced into samples of 2 cm thickness from the surface down to 50
202 cm in depth, and dried at 55°C. Sedimentation rates, and the ages of the different layers

of sediments were determined using the ^{210}Pb method following the Constant Rate Supply (CRS) model (Appleby and Oldfield, 1978).. The activity of unsupported ^{210}Pb was obtained from the measurements of total ^{210}Pb and ^{226}Ra. ^{226}Ra was measured by gamma spectrometry through the emissions of ^{214}Bi and ^{214}Pb, employing a coaxial HP Ge detector with an energy resolution of 2 keV at 1332 keV, and a relative efficiency of 20%. With the object of determining the activity concentration of total ^{210}Pb, in secular equilibrium with ^{210}Po, the latter was measured using alpha spectrometry. The analysis by alpha-particles was performed with a CANBERRA Alpha spectrometer. ^{210}Po was extracted from the samples using the TBP radiochemical method and its subsequent auto-deposition on silver disks in a thermostatic bath (Martin and Handcock, 2004). Finally, the CRS method was applied for calculating the sediment accumulation rates and for stablishing the geochronology. Detailed method and model descriptions are presented in Ligero et al. (2010; 2002).

3. Results

3.1. Sedimentology and mineralogy

Cores collected from the inner Cadiz Bay during the first coring campaign contain mud, clayey mud and minor silt, and sandy silt with bioclastic shell horizons (Table 1, Figure 2) [insert Figure 2.]. Mineralogical compositions, sedimentary structures, and bioclastic components show no clear downcore patterns, but colour and granulometry define three

223 stratigraphic units from top to bottom. Unit H1 has a black colour, muddy texture, and
224 few shells. Unit H2 is characterized by variable texture, with sand, cobbles, and many
225 shells. Unit H3, which only occurred clearly in sampling site 3, is similar to Unit H1 in
226 texture, but is light grey in colour.
227 The mineralogical composition of the sediments is homogeneous along the cores and
228 similar in the three sampling sites, showing a siliciclastic nature with abundant
229 carbonate (Table 2). Five geochemical profiles were selected to provide an
230 interpretation of the visible lithological subdivision in cores 1MB09, 2MB09 and
231 3MB09 (Table 1, Figure 2). The proportion of fine-grained sediment relative to the total
232 faction (%) declines markedly in layers with higher shell contents. This percentage,
233 estimated from mineralogical composition, is obtained by the ratio of clay mineral
234 content (representing the fine-grained fraction) and the sum of clays plus four phases
235 commonly present in the coarse-grained fraction (quartz, feldspar, plagioclase and
236 heavy minerals). The Sr/Ca and Zr/Rb ratios (XRF core scanning) increase in
237 carbonate-rich layers, and show an inverse pattern to the fine-grained fraction. The
238 layers with high carbonate contents occasionally show bluish-black spots (10B 2.5/2)
239 that could be related to organic matter accumulation. The Ca/Fe ratio (XRF core
240 scanning) shows a pattern very similar to the lithologically determined stratigraphic
241 units, and increases from the onset of Unit H2 towards the bottom of the core in

242 sampling sites Z1 and Z2. The Mn/Rb ratio increases in layers with carbonate shells
243 and/or bluish-black spots.

244 **Table 2.**The maximum, minimum and mean concentrations of major minerals (%). For minor minerals, which were
245 not always detected, we report only the maximum values.

246

Zone		Major minerals					
		Clay minerals	**Quartz**	**Orthoclase**	**Albite**	**Calcite**	**Minor minerals**
Z1	mean	42 (27-54)	15	4	6	24	Gypsum (<9), Aragonite (<4), Ankerite (<4), Dolomite (<3), Apatite (<1)
	maximum	54	29	13	21	48	Halite (<2), Pyrite (<5)
	minimum	27	8	2	2	17	
Z2	mean	37 (23-48)	15	5	5	29	Gypsum (<6), Goethite (<1), Aragonite (<6), Dolomite (<6), Apatite (<1)
	maximum	48	28	13	11	50	Halite (<2), Pyrite (<6)
	minimum	23	10	2	3	18	
Z3	mean	45 (32-58)	10	6	5	22	Gypsum (<5), Goethite (<1), Rutile (<2), Barite (<4), Aragonite (<5), Ankerite (<1)
	maximum	58	24	26	7	36	Dolomite (<3), Apatite (<7), Halite (<2), Pyrite (<6), Hematite (<1)
	minimum	32	5	3	3	15	

247

248

249

250

251

252 *3.2. Elemental composition*

253 Trace metal and lithogenic element concentrations (ICP-OES) are higher in Z1 than in
254 Z2 (Table 3). Fe, Mn, P, V, Cu and Zn contents were normalised to Al and are
255 presented in Figure 3 [insert Figure 3.]. Fe/Al and V/Al ratios do not show consistent
256 patterns of change with depth at any of the sample sites. However, Cu/Al and Zn/Al
257 ratios decrease steadily towards to the bottom of the core, particularly over the
258 uppermost 60 cm. Mn/Al ratios decrease strongly in the first 5 cm at both sites, but
259 increase more steadily from 5 to 30 cm depth. Interestingly, in the layer between 35 and
260 65 cm depth, there are pronounced differences in the Mn/Al ratios at both sites (much
261 higher Mn/Al in Z2). P/Al ratios are similar in both sites at the core tops, and decreased
262 over the top 5 cm in both cases. However, below the uppermost 15 cm, the P/Al ratio in
263 Z2 tends to be consistent higher than in Z1, with a major P/Al peak at 40 cm depth in
264 Z2.

265 High-resolution vertical profiles of element distributions and ratios by XRF core
266 scanning are shown in Figure 4 [insert Figure 4]. The Al and Ti profiles show an
267 increase towards the bottom of the cores at both sites, whereas Cl shows an inverse
268 trend. These inverse patterns between Cl and both Al and Ti in XRF core scanner
269 measurements on wet sediment are usually attributed to variations in interstitial water

270 **Table 3.**The maximum, minimum and mean concentrations of heavy metals and lithogenic elements.

271 Concentrations are expressed in mg g-1 (dry weight) for Al, Fe, Mn and P, and μg g^{-1} (dry weight) for Cd, Cr, Cu,

272 Ni, Pb, V and Zn. Zero values were not included to calculate the maximum, minimum and mean (only for Pb).

273

Zone		Al	Fe	Mn	P	Cd	Cr	Cu	Ni	Pb	V	Zn
Z1	mean	59.3	28.1	0.392	0.625	2.05	77.03	46.3	37.7	25.7	99.6	96
	maximum	67.7	32.3	0.471	0.822	4.28	101.7	73	67	41.9	115.2	153.7
	minimum	48.5	24.2	0.298	0.476	1.31	58.1	23.3	24.2	11.7	80.7	64.2
Z2	mean	36.7	16.5	0.336	0.435	1.35	65.4	27.2	18.9	14.8	60.6	65.6
	maximum	61.2	29.5	0.602	0.625	2.27	98.7	40.9	36.4	33.3	106.9	105.1
	minimum	22.9	9.2	0.224	0.305	0.49	46.4	12.8	10.6	5.7	32.8	38.1

274

275

276

277

278 contents along the core (Tjallingii et al., 2007). The water content of the sediment
279 diminished from the top of the core down to 25 and 40 cm depth for Z1 and Z2,
280 respectively (see supplementary material). Thus, neither Al nor Ti derived from XRF
281 core scanning can be utilized as a normalizing parameter for the terrigenous fraction in
282 our study. Such corrections are necessary, however, to eliminate the effects of grain-size
283 variations and variable dilution factors (e.g., by organic C or carbonate) on element
284 profiles, so that unbiased records of diagenetic and anthropogenic processes can be
285 generated (Calvert and Pedersen, 2007; Martinez-Ruiz et al., 2015). We use Rb instead
286 of Al or Ti, because it is a detrital element present in feldspars and phyllosilicates (both
287 abundant components in the studied deposits; Table 2), and it is less affected by
288 physical effects during XRF scanning due to its higher atomic mass (Rothwell et al.,
289 2006).
290 The Ca/Fe ratio increases markedly from 35 cm depth in Z2, while this increase
291 is more gradual and begins at 70 cm depth in Z1 (Figure 4). This index marks the
292 transition between the H1 and H2 stratigraphic units. Zr/Rb and Sr/Ca ratios show
293 enrichments at the same depths, especially in Z2. The Mn/Rb profile is constant in Z1
294 and displays an increase between 30 and 60 cm depth in Z2. The Pb/Rb ratio decreases
295 towards the sediment bottom in both sites. Nevertheless, the Ni/Rb profile is fairly
296 constant throughout the core.
297

298 *3.3. Iron speciation*

299 The vertical profiles of each Fe fraction relative to the highly reactive Fe (Fe_{HR}) are
300 similar at both sites (Figure 5) [insert Figure 5]. The Fe_{mag}/Fe_{HR} ratios remain relatively
301 constant throughout the cores, with values close to 0.1. The $Fe(III)_{HFO}/Fe_{HR}$ and
302 Fe_{ox}/Fe_{HR} ratios are elevated in the uppermost 10 and 30 cm, respectively. The
303 $Fe(II)_{red}/Fe_{HR}$ ratio is also highest in the uppermost 30 cm, whereas the Fe_{sulf}/Fe_{HR} ratio
304 increases below 30 cm depth. The $Fe(II)_{red}/Fe_{HR}$ profile in Z1 has two peaks at 8 and 25
305 cm depth, and the Fe_{sulf}/Fe_{HR} profile has a broad maximum around 15 cm depth in both
306 Z1 and Z2. Below 30 cm depth, all Fe fractions and ratios remain relatively constant,
307 and over 80% of the Fe_{HR} in the sediment is ultimately bound as Fe_{sulf} (i.e., pyrite).
308

309 *3.4. C-N compositions*

310 The C_{org} content of the sediments is higher in Z1 than in Z2, with mean values of 2.3
311 and 1.3 wt%, respectively (Figure 6). [insert Figure 6] The C_{org} profiles show a general
312 decreasing trend from the top of the core down to 40 cm depth in both sampling
313 locations. Between 40 and 75 cm depth, Z2 displays a high-C_{org} layer that is absent from
314 Z1. In Z1, C_{org} consistently increases from 55 cm depth to the bottom of the core. The
315 carbonate contents are generally higher in Z2 than in Z1, with mean values of 14.5 and
316 8.7 wt%, respectively. This difference is higher at the bottom of the cores. In Z2, a layer
317 from about 30 to 65 cm depth shows variable carbonate contents, reaching 25 wt%.

318 The molar C_{org}/N ratio increases progressively towards the bottom of both cores,
319 ranging from values around 10 to around 20 at ~75-80 cm depth (Figure 6). Below this
320 depth, C_{org}/N ratios remain relatively constant. The molar C_{org}/N ratios are slightly
321 higher for Z1 than for Z2, with mean values of 16.7 and 14.5, respectively.
322
323 *3.5. Stable C and N isotopes*
324 The depth profiles for $\delta^{13}C$ and $\delta^{15}N$ in sedimentary organic matter (OM) display
325 enrichments in the heavier isotope at the core tops, mainly in the upper 40 cm (Figure
326 7). [insert Figure 7] As observed for other geochemical variables, the $\delta^{13}C$ profile
327 displays more scatter in Z2. At this sampling site, $\delta^{13}C$ shows a marked depletion from
328 about 40 to 65 cm depth.
329
330 *3.6. Chronology*
331 The vertical profile of unsupported ^{210}Pb shows an exponential decay with depth (see
332 supplementary material). The determination coefficients' values for the exponential fit
333 are 0.835 and 0.685 for Z1 and Z2, respectively. However, the flattening of the natural
334 log of $^{210}Pb_{ex}$ near the surface indicates a mixed layer of about 10 cm depth in both
335 cores. This surficial mixing does not totally invalidate the use of $^{210}Pb_{ex}$ profile but the
336 CRS model-estimated ages should be considered approximate (Johannessen and

337 Macdonald, 2012). Dating was performed down to 46 cm depth for sampling site 1 and
338 to 42 cm depth for sampling site 2 (see supplementary material).
339 The ^{210}Pb-based chronology indicates that sediment accumulation rates changed
340 over time, with a general increase since the early 1930's to the present (Figure 8).
341 [insert Figure 8] During this period, the sedimentation rates increased 4.2-fold and 3.6-
342 fold for Z1 and Z2, respectively. However, sediment accumulation rates were relatively
343 constant for the period 1875-1930, with an average linear sedimentation rate of 0.13 cm
344 y^{-1}. This sedimentation rate allows us to complete the age-depth model for the
345 equivalent sedimentary facies downcore, assuming that below the maximum depth of
346 dating the sedimentation rate is constant, as no sedimentological changes or variations
347 in dry bulk density occur down to the bottom of the core (see supplementary material).
348 In addition, the geochronology can only be applied to unit H1, given that unit H2 has a
349 different lithology (Figure 4). Thus, age-element and element ratio profiles can be
350 extrapolated to 70 cm at Z1, but only down to 30 cm at Z2. Nevertheless, the estimated
351 ages at Z1 below the maximum depth of dating, and the estimated rates of sediment
352 accumulation in the mixed area of both sampling sites, must be interpreted with caution.
353
354 **4. Discussion**
355 *4.1. Environmental interpretation based on changes in lithology and XRF core scanning*

356 Here, we compare the sedimentary units (Figure 2) defined in this study with the
357 distribution of relict and modern facies in Cadiz Bay, and also the lithofacies present in
358 the Holocene record. Unit H1, at the top of core, has a black colour as a consequence of
359 FeS, FeS_2, and organic matter accumulation. The fine-grained nature of this unit and the
360 presence of bivalve shells at certain depths is consistent with the predominant facies
361 found in recent sediments of the area (Achab et al., 2000; Gutiérrez-Mas et al., 1997).
362 The carbonate-rich poorly sorted mud, sand, and gravel of unit H2 is consistent
363 with coarser-grained facies that are usually found near cliffs and rocky bottoms in Cadiz
364 Bay (Achab et al., 2000; Gutiérrez-Mas et al., 1997), but here, the coarser sediments are
365 mixed with fine sediments. Similar deposits are found in recent lithofacies of the outer
366 Cadiz Bay and surrounding marshes, and their formation is related to sporadic high-
367 energy events (Gutiérrez-Mas et al., 2009; Lario et al., 2002). The similar sedimentary
368 characteristics of unit H3, relative to H1, suggest deposition under quiet conditions in a
369 low energy environment. At present, such conditions govern the inner Cadiz Bay.
370 Therefore, unit H2 represents an interruption of the normal depositional regime.
371 Besides the lithological contrast, the onset of unit H2 is recognized by higher
372 Sr/Ca and Zr/Rb ratios (Figure 2). We attribute the higher Sr/Ca ratio to the abundance
373 of shells containing high-Sr aragonite, although this ratio can also be affected by
374 variations in porosity and sediment grain-size (Croudace et al., 2006; Rothwell et al.,
375 2006; Thomson et al., 2006). In this work, the Sr/Ca ratio shows an inverse pattern in

relation to the proportion of fine-grained material, and a similar pattern to the Zr/Rb ratio (Figure 2). The Zr/Rb ratio is usually high in coarser sediments (Croudace et al., 2006), indicating that shell accumulations are associated with the coarser-grained fraction of sediment. In Z1 and Z2, a gradual downcore increase in the Ca/Fe ratio within this unit is also observed (Figure 2). The Ca/Fe ratio is a useful proxy for sediment grading and recognition of sedimentary units (Rothwell et al., 2006); this parameter reflects changes in the detrital composition, indicating the relative abundance of biogenic carbonate and clay. The higher carbonate compared to clay content within unit H2 increases the Ca/Fe ratio, given that Fe content in the sediment remains invariant with depth (see Fe/Al profile for the second cruise; Figure 6a). Therefore, the Ca/Fe ratio, in combination with Sr/Ca and Zr/Rb ratios, allows us to distinguish unit H1 from unit H2 (Figure 4).

The most reasonable cause for the appearance of unit H2 (i.e. the shell horizon) in Z2 and Z3 is the construction of a port between 1948 and 1953 AD. These dates match with the age of the top of unit H2 in the station closest to the port (AC 1946 ± 2 years in Z2). For its construction, 500,000 m^3 of sediment from the bay bottom was retrieved and 6 km^2 of sea was filled up with blocks, gravel and sand. In the Oslo port, Lepland et al. (2010) found deposits from previous fillings (and dredging activities) at almost 500 m distance from the docks and along the navigation channel. Therefore, unit H2 in Z2 and Z3 likely originated during the construction operations given the proximity of these

396 sampling sites to the port (Figure 1). The textural features (and geochemical properties)
397 of unit H2 can be explained by the re-working of sediment and its mixture with sandy
398 sediments rich in shells from the outer Cadiz Bay that were used as filling material.
399 The origin of unit H2 at Z1 is not known, although it occurs earlier than Z2 and
400 Z3. Site Z1 is located far away from any current port but it is surrounded by smaller
401 channels of anthropogenic and natural origin (Figure 1). Since this area has been a
402 maritime port for centuries and dredging activities have been taking place since the 17th
403 century in Cadiz Bay, unit H2 at Z1 could be the product of some older canalization or
404 abandoned dock. Based on the above, unit H2 is an anthropogenic deposit rather than a
405 natural lithofacies at all sites. In addition, the sediment is very mixed and post-
406 depositional alteration is very likely within this unit. Thus, it is not possible to
407 reconstruct the environment from the onset of unit H2 downwards.
408
409 *4.2. Speciation of Fe in Cadiz Bay*
410 Until now, all studies on iron speciation in Cadiz Bay have focused exclusively on its
411 role as a potential pollutant (Izquierdo et al., 1997; Morillo et al., 2007; Sáenz et al.,
412 2003). However, here, the partitioning of Fe is used as a tracer of diagenetic processes.
413 The availability of reactive Fe controls pore water chemistry (Canfield, 1989) and OM
414 burial (Lalonde et al., 2012) in marine sediments. Hence, the role of Fe biogeochemistry
415 during early diagenesis can aid interpretation of sedimentary records. The marked

decrease in $Fe(III)_{HFO}/Fe_{HR}$ and Fe_{ox}/Fe_{HR} in the uppermost part of the sediment profile could, at least in part, be due to reaction with hydrogen sulphide released during organic matter decomposition by bacterial sulphate reduction (BSR), although dissimilatory Fe reduction (DIR) also likely contributes to Fe (oxyhydr)oxide dissolution (Figure 5). The reactivity of Fe(III) minerals towards H_2S (and DIR) depends on the mineral phase and its crystallinity, with $Fe(III)_{HFO}$ being the most reactive Fe fraction (Canfield 1989, Canfield et al. 1992, Poulton et al. 2004). In contrast, the Fe_{mag} /Fe_{HR} profile remains constant throughout the sediment record, suggesting that Fe_{mag} does not react rapidly with H_2S and is not significantly affected by DIR (see Canfield and Berner 1987), although this could also be countered by biogenic magnetite production (Lovley et al., 1987). The Fe_{sulf} pool (mainly pyrite) increases simultaneously with the reductive dissolution of Fe(III) phases down to 30 cm depth, below which the Fe (oxyhydr)oxide and pyrite profiles remain relatively constant. Because highly reactive Fe (oxyhydr)oxides are still available below this depth, it appears likely that the availability of labile OM is the limiting constraint on further reductive dissolution at depth in the sediment column. It is generally assumed that there is a gradual decrease in the amount of labile OM and a corresponding increase in the amount of refractory OM with increasing sediment depth (Middelburg et al., 1993).The labile fraction of a mixed OM pool seems to be largely degraded in the uppermost 30-40 cm (Figure 6a), while below this depth mostly the refractory fraction remains. The presence of highly reactive Fe

436 (oxyhydr)oxides down to 30 cm depth could be a combination of two factors. On the
437 one hand, sedimentation rates are high in Cadiz Bay (Figure 8) so reactive Fe(III)
438 minerals may have escaped reductive dissolution by passing through the zones of iron
439 and sulphate reduction quickly. On the other hand, only the most reactive Fe
440 (oxyhydr)oxides react with H_2S on relevant timescales (hundreds of years), while other
441 Fe(III) minerals can take much longer to become sulphidised (Poulton et al., 2004b). So
442 the presence of relatively stable levels of C_{org} and Fe (oxyhydr)oxides in the deeper part
443 of the sediment record indicates that further degradation of both components has been
444 stalled due to their rather refractory nature.
445
446 *4.3. Estimation of the original input of organic carbon to the Cadiz Bay sediments*
447 The upcore increase in C_{org} (Figure 6a) observed in the sediments of our study could
448 indicate an increase in OM input in recent times due to higher biological productivity.
449 However, this apparent increase in C_{org} could also be a result of microbial
450 mineralization downcore. Consequently, the C_{org} content in these sediments cannot be
451 directly used as proxy of biological productivity in the past. Instead, we estimate the
452 original input of C_{org} to the bottom sediments from the water column by using the iron
453 speciation data in combination with the C_{org} content of the sediment.
454 Considering that the loss of C_{org} in the shallow water column in our system is
455 negligible, the original input of C_{org} to the bottom sediments (OC_{orig}) can be

theoretically estimated from the amount of C_{org} preserved in the sediment (i.e. the C_{org} content measured at every depth), plus the mineralised C_{org} (C_{min}) during the time of deposition (i.e., $OC_{orig} = C_{min}+C_{org}$). Here, we infer C_{min} from the content of Fe present as pyrite (Fe_{py}). Pyrite in modern sediments forms at the expense of C_{org} degraded via microbial reduction of sulphate (Berner, 1984) and, therefore, the content of pyrite measured in the sediment can be expressed in respired C_{org} equivalents. The net equation involving the mineralization of C_{org} (assuming a simple CH_2O composition for C_{org}) by BSR can be described as:

$$2CH_2O + SO_4^{2-} \rightarrow 2HCO_3^- + H_2S \quad (1)$$

The H_2S released into the pore water by this reaction may be trapped in the solid phase, mostly by reacting with iron minerals to form pyrite (FeS_2). In recent marine sediments, the trapping in the form of pyrite typically accounts for 5-20 % of the total H_2S production (Jorgensen and Kasten, 2006). Pyrite is very stable, resulting in its permanent burial in the long-term. This process can be expressed by the following bidirectional equation, according to Berner & Canfield (1989):

$$2Fe_2O_3 + 16Ca^{2+} + HCO_3^- + 8SO_4^{2-} \leftrightarrow 15O_2 + 4FeS_2 + 16CaCO_3 + 8H_2O \quad (2)$$

The equation reflects the global effect of sulphur cycle on atmospheric O_2 concentration and reading it from react to product side represents the net burial of sedimentary pyrite. Interestedly, this equation allows us to calculate the amount of sulphate that has been microbially respired and effectively trapped in the solid phase since BSR is the main

476 mechanism for removing sulphate from the oceans in modern sediments (Jorgensen and
477 Kasten, 2006). According to equation 2, for every four moles of FeS_2 buried, eight
478 moles of SO_4^{2-} are reduced, whereas according to equation 1 the biological reduction of
479 one mole of SO_4^{2-} mineralizes two moles of CH_2O. If both equations are combined, for
480 every mole of FeS_2 formed, four moles of CH_2O are mineralized by BSR. In coastal
481 sediments, sulphate reduction typically accounts for 25-70% of the total C_{org}
482 mineralization (Canfield et al., 1993; Crill and Martens, 1987; Jorgensen, 1982). Thus,
483 if we assume that BSR accounts for 50% of the total respiration on average, C_{min} is
484 approximately double the C_{org} respired by BSR. Therefore, for every mole of FeS_2
485 formed, eight moles of CH_2O are mineralized.

486 The proposed way of calculating C_{min} is limited in several ways. On the one hand,
487 the use of sedimentary pyrite content as an estimation of the C_{min} would be valid only in
488 systems where iron sulphides other than pyrite are minor and where pyrite formation is
489 limited by the availability of labile C_{org}. In our system, pyrite is indeed the main iron
490 sulphide, representing > 90% of this mineral phase in all samples (an average value of
491 99% for both sampling sites). In addition, as already discussed (see section 4.2), there is
492 no evidence for a limitation of pyrite formation by iron or sulphur, such that in Cadiz
493 Bay sediments all degradable C_{org} is available for pyrite formation, reinforcing our
494 assumption.

495 On the other hand, sedimentary pyrite formation is more complex than is assumed here,
496 involving chemical reactions in several steps (Jorgensen and Kasten, 2006). However,
497 several pathways of pyrite formation have been reported in the literature and, therefore,
498 results would vary highly depending on the pathway selected. In contrast, our
499 calculation uses a relationship between two components from a mass balance equation
500 which is known to have remained constant over recent times. Also, models including
501 equation 2 were able to reproduce carbon cycle past dynamics (e.g. Berner, 2006),
502 indicating its reliability. Finally, the contribution of BSR to the total sediment
503 respiration may be different to 50% and may have varied over time. Nevertheless, our
504 approach offers a first order estimation of OM degradation (in the absence of direct
505 measurements of OM diagenesis for the study area), and gives an acceptable solution
506 for the reconstruction of OC_{orig} input despite of the uncertainties in the calculation of
507 C_{min}.

508 For all above reasons, OC_{orig} is applied in the last section as a tentative indicator
509 of the evolution of the productivity in the water column and as tracer of anthropogenic
510 OM inputs in the inner Cadiz Bay.

511

512 *4.4. Organic geochemical proxies for tracing environmental changes in Cadiz Bay*

513 C_{org}/N ratios at the sediment surface (8-12; Figure 6c) indicate a predominantly
514 algal origin for the sedimentary OM (Meyers, 1997, 1994). The increase in this ratio

515 with sediment depth may be related both to changes in OM sources and to differential
516 OM decomposition after sedimentation. Given that this trend continues beyond the most
517 active remineralization zone (first 30 cm depth; see section 4.2) and continues down to
518 70-80 cm depth, the C_{org}/N ratio most likely reflects variations in OM sources rather
519 than post-depositional alteration. In Z2, low C_{org}/N ratios (close to 5; Figure 6c) occur at
520 certain depths with C_{org} contents below 0.5% (Figure 6a). Such low C_{org}/N ratios occur
521 in C_{org}-poor sediments caused by sorption of ammonium and organic nitrogen within
522 clay minerals (Müller, 1977), preventing its use as indicator of OM origin under similar
523 conditions. In our study the low C_{org}/N ratios occur within unit H2 (see Figure 4) and,
524 therefore, these values are not considered in the environmental reconstruction for Z2.
525 The values of $\delta^{13}C$ and $\delta^{15}N$ obtained in the studied sediment (between -22 and -
526 17‰ in $\delta^{13}C$ and 4-7‰ in $\delta^{15}N$; Figure 7) suggest that the sedimentary OM is
527 predominantly of marine origin, in agreement with the C_{org}/N ratios (Lamb et al., 2006;
528 Meyers, 1994; Montoya, 2007). Again, the observed increase in $\delta^{13}C$ and $\delta^{15}N$ values
529 from 30 cm depth to the top of the cores could be related both to environmental changes
530 (e.g. changes in the vegetation, productivity, or pollution) and to diagenetic changes.
531 As diagenetic processes can alter the primary isotopic composition of OM (Gaye-Haake
532 et al., 2005; Lehmann et al., 2002; Macko and Estep, 1984), the applicability of $\delta^{13}C$
533 and $\delta^{15}N$ as tracers of environmental changes is currently a matter of debate (see
534 reviews of Lamb et al. 2006 and Robinson et al. 2012). Nevertheless, several studies

535 indicate that their values in the bulk sediment can be used to reconstruct environmental
536 changes in the water column despite diagenetic overprints (Freudenthal et al., 2001;
537 Kohzu et al., 2011; Möbius, 2013). The variability in $\delta^{13}C$ and $\delta^{15}N$ caused by
538 diagenesis is small in comparison with the isotopic variation due to environmental
539 change. Therefore, the upcore increase in $\delta^{13}C$ and $\delta^{15}N$ values (Figure 7) likely
540 represent temporal changes in the OM sources entering in the inner Cadiz bay, and
541 possible changes in the trophic state of the water column.

542

543 *4.5. Minor and trace elements in Cadiz Bay sediments*

544 The contents of heavy metals and lithogenic elements (Table 2) in the studied
545 sediments are generally in the range of other studies performed in the area (Carrasco et
546 al., 2003; Gomez-Parra et al., 1984; Morillo et al., 2007). The lower values observed in
547 Z2, compared to Z1, are consistent with the higher proportion of carbonates at this
548 station (Figure 6b), thus diluting the elements present in the terrigenous fraction.

549 The invariant profiles of Fe/Al, V/Al and Ni/Rb (Figures 3a, 3d and 4) indicate
550 that these metals are largely controlled by terrigenous input. Furthermore, the fact that
551 redox-sensitive elements such as V or Ni (Tribovillard et al., 2006) show constant
552 profiles indicates that the column water in Cadiz Bay was never anoxic during the
553 studied time period. In contrast, the increases in Cu/Al, Zn/Al and Pb/Rb ratios at the
554 core top (Figures 3e, 3f and 4) seem to represent inputs of heavy metals from

555 anthropogenic sources. In Cadiz Bay, these metals (Cu, Zn, Pb) are frequently linked to
556 urban and industrial contamination (Carrasco et al., 2003; Gomez-Parra et al., 1984;
557 Morillo et al., 2007). However, Cu, Zn and Pb are metals which may potentially
558 undergo early diagenetic mobilization in the sediment (Spencer et al., 2003). To discard
559 this possible alteration, we consider these heavy metals in relation to the Fe oxide
560 ($Fe(III)_{HFO}$ +Fe_{ox}) and Fe sulfide contents (Fe_{sulf}) obtained from Fe partitioning (see
561 section 2.8). In Cadiz Bay sediments, Fe (oxyhydr)oxides are the main scavengers of Zn
562 and Pb, whereas Cu is strongly controlled by sulphides (Morillo et al., 2007). The weak
563 correlation between the concentration of these metals and their corresponding
564 scavengers (r=0.41, r=0.47 and r=0.42 for Zn, Pb and Cu, respectively) demonstrates
565 that diagenetic mobilization has not significantly affected the distribution of Cu, Zn and
566 Pb in the sediment.
567 Changes in the Mn/Al and P/Al ratios along the cores (Figures 3b and 3c) are
568 probably related to post-depositional processes involving dissimilatory reduction of Mn,
569 Fe and sulphate during diagenesis of OM (Spencer et al., 2003; Tribovillard et al.,
570 2006). In modern marine sediments, Mn-oxyhydroxides and Mn-carbonates are known
571 to be formed diagenetically within the sediment (Calvert and Pedersen, 1996, 1993).
572 Although we did not study Mn speciation in our cores, the increased Mn/Al ratio in the
573 uppermost 5 cm could indicate accumulation of Mn-oxyhydroxides in the surface, as a
574 consequence of dissimilatory Mn reduction at depth followed by dissolved Mn diffusion

575 and re-precipitation at the sediment surface. Conversely, the slight downcore increase in
576 the Mn/Al ratio observed in the top 30 cm (Figure 3b) may indicate formation of
577 authigenic Mn-carbonates at depth, as a consequence of the high alkalinity derived from
578 BSR and DIR. The slight decrease in P/Al with depth (Figure 3c), on the other hand, is
579 probably due to P being released to the dissolved phase during OM diagenesis, then
580 either being adsorbed to carbonate minerals or precipitated as authigenic apatite
581 (Ruttenberg and Berner, 1993). This decrease is consistent with the typical pattern for
582 total P and organic P in Cadiz Bay sediments (Ponce et al., 2010).
583 In Z2, a clear peak in the P/Al ratio between 30 and 40 cm depth is observed,
584 exactly at the top of a carbonate rich high-Mn layer located between 35 and 65 cm depth
585 (Figures 3b, 3c and 6b). The observed increase in the Mn/Al ratio (c.f. Figure 3b and
586 6b) may reflect the formation of authigenic Mn carbonates at these depths as a
587 consequence of their precipitation on pre-existent biogenic carbonates (Boyle, 1983).
588 Also, the high P/Al ratio (c.f. Figure 3c and 6b) may indicate authigenic apatite
589 formation and/or adsorption of P onto carbonate particles. The diagenetic formation of
590 apatite (carbonate fluorapatite) and the sorption of P on carbonates are processes very
591 common in marine sediments (Ruttenberg and Berner, 1993; Slomp et al., 1996). Thus,
592 the carbonate-rich interval seems to be the most significant factor leading to
593 enrichments in Mn and P at this station.

In summary, only the ratios of Cu/Al, Zn/Al and Pb/Rb are applied in the following section as promising tracers of heavy metal contamination in Cadiz Bay. Moreover, given the intense diagenetic mobilization of Mn, the ratios of Mn/Al and Mn/Rb should not be utilized as a proxy for redox conditions in the water column.

4.6. Trends in ecological conditions in Cadiz Bay over the past few centuries

Sedimentary records of several variables indicative of urban and industrial activities, indicators of OM sources, and tracers of eutrophication and productivity, were dated using the age-depth model determined for H1 (see section 3.6) to determine their historic evolution since 1680 in Z1, and since 1940 in Z2 (Figure 9) [insert Figure 9].

Human population in the Cadiz Bay area remained stable at around 200,000 inhabitants between 1787 and 1910, increasing rapidly to 700,000 at present. This population increase can be used as a proxy of historic anthropogenic impacts on the ecosystem and sediments. In addition, 1910 AC marks the onset of the industrial period for inner Cadiz Bay and, therefore, records prior to this date could represent more pristine conditions of the bay.

The inner Cadiz Bay has been progressively filled up with sediment over the last few centuries (Figure 8). In addition, sediment accumulation rates have accelerated several-fold since the 1930s. Present rates of sediment accumulation range from 0.5 to 1 g cm^{-2} y^{-1}, being 3 to 7 times higher than those found before the 1930s. This increase

614 has occurred despite the construction of six dams in the main rivers draining into the
615 wider Cadiz Bay since the 1960s, which is known to decrease sediment load to the
616 coastal areas (Syvitski et al., 2005). The exponential population growth and the
617 extensive transformation of the area due to urbanization, deforestation, and agricultural
618 activities, all of which increase soil erosion and sediment transport via rivers (Syvitski
619 and Milliman, 2007), have more than compensated for the decrease caused by
620 damming. Moreover, a higher confinement of the water body as a consequence of
621 desiccation of old marshes, and construction of ports, drawbridges, and other maritime
622 structures in Cadiz Bay, have also contributed to the increase in sediment accumulation
623 during the 20th century. Although the increase in these rates is observed to a large extent
624 within the mixed zone of Z1 and Z2 and should be interpreted with caution, this
625 tendency actually starts at depths well below the mixing zone (see supplementary
626 material) indicating its validity. However, further studies with validation methods of Pb-
627 210 dating are needed to corroborate this tendency in the area.
628 The heavy metal content normalised to the terrigenous fraction (Zn, Cu, and Pb)
629 has increased since the 1930s (Figure 9), in agreement with previous historical studies
630 on metal contamination in the area (Ligero et al. 2002, 2004). Ratios of Zn/Al and
631 Cu/Al increased notably from 1930 to 1970, remaining more constant, or even
632 decreasing (in Z2), since the 1980s. However, Pb/Rb ratios increased from the 1970s in
633 Z1, and even from 1940 in Z2, up to the mid-1990s. These changes in heavy metal

634 contamination clearly reflect the evolution of urban development, including increased
635 road traffic (for Pb), and of the industrial activity (mainly naval) in the area (Gomez-
636 Parra et al., 1984; Ligero et al., 2004, 2002; Ponce et al., 2000). In addition these results
637 suggest that levels of contamination in the inner Cadiz Bay were higher between 1970
638 and the mid-1990s.

639 Zinc, copper and lead are metals widely used in paint as anti-corrosion and anti-
640 fouling agents in shipbuilding. The rapid increase in Zn/Al and Cu/Al ratios in the
641 1950s coincides with the peak in activity of the naval industry; the subsequent decrease
642 in the 1980s corresponds with the closure of the naval industry in the area and its
643 transformation to automobile and aerospace manufacturing (Figure 9). Conversely, the
644 existence of other sources for Pb, such as atmospheric car contamination (Gomez-Parra
645 et al., 1984; Ligero et al., 2004) or urban effluents (Ponce et al., 2000), can explain the
646 different temporal evolution of the Pb/Rb ratio in comparison to Zn/Al and Cu/Al ratios.
647 The introduction of unleaded gasoline at the end of 1980s significantly reduced
648 contamination by this metal in Cadiz Bay in the following years (Ligero et al., 2004);
649 however, an increased input of Pb via urban effluents due to population growth might
650 explain why levels maintained high after the 1990s.

651 The organic carbon content of material that reaches the sediment (OC_{orig}) showed
652 a relatively constant value of 3.7 wt% from 1680 until the early 20th century in Z1
653 (Figure 9). Thereafter, OC_{orig} increased slightly towards values > 4 wt% during the first

654 half of the 20th century, which was probably caused by the increase in human
655 population. Since then, OC_{orig} has remained constant despite an almost 3-fold increase in
656 human population in the Cadiz Bay area (from 230,000 inhabitants in 1930 to 700,000
657 inhabitants in 2011). Similarly, OC_{orig} in Z2 shows a constant value of 2 wt% since
658 1946. Given that the higher values in the first half of the 20th century compared to pre-
659 1900s persist, this signifies that most of this C_{org} was autochthonous, produced within
660 the inner bay by primary producers, and there was little input of anthropogenic organic
661 material from land.

662 Available water column chlorophyll measurements in the inner Cadiz bay only go
663 back as far as 1967 (Establier et al., 1990; Muñoz Perez and Sánchez de LaMadrid Rey,
664 1994). These data do not indicate any clear or significant increase in primary production
665 for the period between 1967 and 1990. Our results also suggest that pelagic productivity
666 in the inner Cadiz bay has remained constant during the 20th century. Benthic primary
667 producers like seagrasses and *C. prolifera*, on the other hand, play an important role in
668 the overall primary production of the inner bay and contribute significantly to the C_{org}
669 input to the bay (Morris et al., 2009). However, OC_{orig} does not take into account the
670 organic carbon derived from these marine macrophytobenthos. It is likely that benthic
671 primary production has increased over the years as the basin has become shallower in
672 parallel to increased anthropogenic inputs of nutrients.

673 The increase in OC_{orig} since the early 20th century is associated with changes in
674 the composition of the OM as evident by the profiles of C_{org}/N, $\delta^{13}C$, and $\delta^{15}N$ (Figure
675 9). The rather low C_{org}/N ratio in very recent sediments in Cadiz Bay, characteristic of
676 marine primary producers (i.e., micro- and macroalgae) with lower C_{org}/N ratios than
677 terrestrial plants (Meyers, 1997, 1994), and its steady decrease from the early 20th
678 century up to the present, suggest a higher contribution of marine produced C_{org}
679 compared to terrestrial C_{org}. The higher marine C_{org} input could be attributed to either an
680 increase in the autochthonous primary productivity or a decrease in the terrestrial
681 supplies to the inner bay, or both. Given that the Al content of sediment (a proxy for
682 terrigenous supply) has remained relatively constant since the 17th century in Z1 and
683 even increased notably since the 1970s in both stations (Figure 9), the first hypothesis is
684 more plausible. In addition, the increase in sewage discharges over time would reduce
685 the C_{org}/N ratio by increasing the N content in the primary producer biomass (Morris et
686 al., 2009; Wigand et al., 2007). Consequently, an increase of nitrophilic species in the
687 inner Cadiz Bay, such as *C.prolifera* and *Ulva sp.,* has also likely contributed to
688 lowering the sedimentary C_{org}/N ratio.
689 Major changes in $\delta^{13}C$ and $\delta^{15}N$ values in the sedimentary OM also occurred in
690 the early 20th century due to population growth and changes in land use (Figure 9). The
691 $\delta^{15}N$ and $\delta^{13}C$ increased from 5 and -20, respectively, since the early 20th century to >7
692 and -17 in contemporary sediments suggesting an increase in marine primary

productivity due to higher N inputs (Ellegaard et al., 2006; Voss et al., 2000). Inputs of anthropogenic OM from wastewater discharges and organic fertilizer runoff, which is rich in ^{15}N, might be the cause of the increased $\delta^{15}N$ surface values (Kendall et al., 2007). Indeed, Morris et al. (2007) demonstrated that the nutrients from urban and aquaculture effluents in Cadiz Bay were being assimilated by *C. prolifera* and *C. nodosa*, enhancing their $\delta^{15}N$ values. Thus, benthic primary production increased since the early 20th century due to a higher input of nutrients as a consequence of the population increase. Moreover, the contribution of the benthic macroalgae to primary production seems to have increased over this period, as suggested by the C_{org}/N ratio decrease. All of this evidence reasonably suggests a major change in the trophic conditions of the inner Cadiz Bay during the 20th century.

5. Conclusions

Sedimentary records from the inner Cadiz Bay are suitable for reconstructing the recent past of this shallow water environment. However, post-depositional alteration, probably induced by human activities, has created a discontinuity in the sedimentary record, preventing environmental reconstruction from this discontinuity and below. These and other diagenetic overprints were differentiated from variability induced by environmental changes, via the interpretation of sedimentary profiles using multiple geochemical analyses.

713 Our results show that significant environmental changes have taken place in the
714 inner Cadiz Bay during the 20th century. An increase in heavy metal pollution since the
715 1930s, reflected in the normalized depth profiles of Zn, Cu and Pb, in parallel to an
716 increase in sediment accumulation rates, is observed. Changes in the trophic state of the
717 water column were detected over the last century as indicated by the increase in organic
718 matter input to the sediments and variations in C_{org}/N, $\delta^{13}C_{org}$, and $\delta^{15}N$. Given that the
719 population of Cadiz Bay tripled during this period, all these changes can be interpreted
720 as tracers of anthropogenic influence in the area. The results of this study suggest that a
721 multi-proxy approach and the identification of diagenetic alteration are required for
722 detailed environmental reconstructions in coastal sediments.
723

724 **6. Funding**

725 This research was funded by the Ministry of Education and Science, Spain [CTM 2009-
726 10736, CTM2013-43857-R]; and Andalusian Regional Government [P11-RNM-7199].
727 J.L. Jiménez-Arias was funded by a FPI Grant (2010-063) from the University of Cádiz,
728 Spain. E. García-Robledo was funded by Ramon Areces Foundation (Spain). J.
729 Bohórquez was funded by a FPI Grant (BES- 2010-035711) from the Ministry of
730 Education and Science, Spain. S. Papaspyrou was funded by a JAE-Doc fellowship
731 (Programa JAE, JAE-Doc109, Spanish National Research Council) and a Marie Curie
732 ERG action (NITRICOS, 235005, European Union).

733

734 **7. References**

735 Achab, M., 2011. Dynamics of Sediments Exchange and Transport in the Bay of Cadiz
736 and the Adjacent Continental (SW - Spain). In: Dr. Andrew Manning, I. 978-953-
737 307-586-0 (Ed.), Sediment Transport in Aquatic Environments. InTech, p. 332.

738 Achab, M., Gutiérrez-Mas, J.M., Moral Cardona, J.P., Parrado Román, J.M., González
739 Caballero, J.L., López-Aguayo, F., 2000. Diferenciación de facies relictas y
740 actuales en los sedimentos recientes de los fondos de la bahía de Cádiz. Geogaceta
741 27.

742 Appleby, P.G., Oldfield, F., 1978. The calculation of lead-210 dates assuming a
743 constant rate of supply of unsupported 210Pb to the sediment. Catena 5, 1–8.

744 Berner, R.A., 1984. Sedimentary pyrite formation : An update *. Geochim. Cosmochim.
745 Acta 48, 605–615.

746 Berner, R.A., 2006. GEOCARBSULF: A combined model for Phanerozoic atmospheric
747 O2 and CO2. Geochim. Cosmochim. Acta 70, 5653–5664.

748 Berner, R.A., Canfield, D.E., 1989. A new model for atmospheric oxygen over
749 phanerozoic time. Am. J. Sci. 289, 333–361.

750 Boyle, E.A., 1983. Manganese carbonate overgrowths on foraminifera tests. Geochim.
751 Cosmochim. Acta 47, 1815–1819.

752 Calvert, S.E., Pedersen, T.F., 1993. Geochemistry of Recent oxic and anoxic marine
753 sediments: Implications for the geological record. Mar. Geol. 113, 67–88.

754 Calvert, S.E., Pedersen, T.F., 1996. Sedimentary geochemistry of manganese;
755 implications for the environment of formation of manganiferous black shales.
756 Econ. Geol. 91 , 36–47.

757 Calvert, S.E., Pedersen, T.F., 2007. Elemental Proxies for Palaeoclimatic and
758 Palaeoceanographic Variability in Marine Sediments: Interpretation and
759 Application. In: Hillaire–Marcel, C., De Vernal B T, A. (Eds.), Proxies in Late
760 Cenozoic Paleoceanography. Elsevier, pp. 567–644.

761 Canfield, D.E., 1989. Reactive iron in marine sediments. Geochim. Cosmochim. Acta
762 53, 619–32.

763 Canfield, D.E., Berner, R.A., 1987. Dissolution and pyritization of magnetite in anoxic
764 marine sediments. Geochim. Cosmochim. Acta 51, 645–659.

765 Canfield, D.E., Raiswell, R., Bottrell, S.H., 1992. The reactivity of sedimentary iron

766 minerals towards sulfide. Am. J. Sci. 292, 659–683.
767 Canfield, D.E., Thamdrup, B., Hansen, J.W., 1993. The anaerobic degradation of
768 organic matter in Danish coastal sediments: iron reduction, manganese reduction,
769 and sulfate reduction. Geochim. Cosmochim. Acta 57, 3867–83.
770 Carrasco, M., López-Ramírez, J.A., Benavente, J., López-Aguayo, F., Sales, D., 2003.
771 Assessment of urban and industrial contamination levels in the bay of Cádiz, SW
772 Spain. Mar. Pollut. Bull. 46, 335–45.
773 Chen, F., Zhang, L., Yang, Y., Zhang, D., 2008. Chemical and isotopic alteration of
774 organic matter during early diagenesis : Evidence from the coastal area off-shore
775 the Pearl River estuary , south China. J. Mar. Syst. 74, 372–380.
776 Chung, F.H., 1974. Quantitative interpretation of X-ray diffraction patterns. I. Matrix-
777 flushing method of quantitative multicomponent analysis. J. Appl. Crystallogr. 7,
778 519–525.
779 Church, T.M., Sommerfield, C.K., Velinsky, D.J., Point, D., Benoit, C., Amouroux, D.,
780 Plaa, D., Donard, O.F.X., 2006. Marsh sediments as records of sedimentation,
781 eutrophication and metal pollution in the urban Delaware Estuary. Mar. Chem.
782 102, 72–95.
783 Corzo, A., van Bergeijk, S., García-Robledo, E., 2009. Effects of green macroalgal
784 blooms on intertidal sediments: net metabolism and carbon and nitrogen contents.
785 Mar. Ecol. Prog. Ser. 380, 81–93.
786 Covelli, S., Fontolan, G., Faganeli, J., Ogrinc, N., 2006. Anthropogenic markers in the
787 Holocene stratigraphic sequence of the Gulf of Trieste (northern Adriatic Sea).
788 Mar. Geol. 230, 29–51.
789 Crill, P.M., Martens, C.S., 1987. Biogeochemical cycling in an organic-rich coastal
790 marine basin. 6. Temporal and spatial variations in sulfate reduction rates.
791 Geochim. Cosmochim. Acta 51, 1175–1186.
792 Croudace, I.W., Rindby, A., Rothwell, R.G., 2006. ITRAX : description and evaluation
793 of a new multi-function X-ray core scanner. Geol. Soc. London, Spec. Publ. 267,
794 51–63.
795 Deflandre, B., Mucci, A., Gagné, J.-P., Guignard, C., Sundby, B., 2002. Early
796 diagenetic processes in coastal marine sediments disturbed by a catastrophic
797 sedimentation event. Geochim. Cosmochim. Acta 66, 2547–2558.
798 Di Leonardo, R., Cundy, A.B., Bellanca, A., Mazzola, A., Vizzini, S., 2012.
799 Biogeochemical evaluation of historical sediment contamination in the Gulf of
800 Palermo (NW Sicily): Analysis of pseudo-trace elements and stable isotope
801 signals. J. Mar. Syst. 94, 185–196.

802 Ellegaard, M., Clarke, A.L., Reuss, N., Drew, S., Weckström, K., Stephen, J.,
803 Anderson, N.J., Conley, D.J., 2006. Multi-proxy evidence of long-term changes in
804 ecosystem structure in a Danish marine estuary , linked to increased nutrient
805 loading. Estuar. Coast. Shelf Sci. 68, 567–578.

806 Establier, R., Blasco, L.M.J., Gómez-Parra, A., 1990. Fitoplancton e hidrografía de la
807 bahía de Cádiz (SO España) de abril 1986 a diciembre 1988. Sci. Mar. 54, 203–
808 209.

809 Freudenthal, T., Wagner, T., Wenzhöfer, F., Zabel, M., Wefer, G., 2001. Early
810 diagenesis of organic matter from sediments of the eastern subtropical Atlantic :
811 Evidence from stable nitrogen and carbon isotopes. Geochim. Cosmochim. Acta
812 65, 1795–1808.

813 Gaye-Haake, B., Lahajnar, N., Emeis, K.-C., Unger, D., Rixen, T., Suthhof, A.,
814 Ramaswamy, V., Schulz, H., Paropkari, A.L., Guptha, M.V.S., Ittekkot, V., 2005.
815 Stable nitrogen isotopic ratios of sinking particles and sediments from the northern
816 Indian Ocean. Mar. Chem. 96, 243–255.

817 Giralt, S., Rico-Herrero, M.T., Vega, J.C., Valero-Garcés, B.L., 2011. Quantitative
818 climate reconstruction linking meteorological , limnological and XRF core scanner
819 datasets: the Lake Sanabria case study , NW Spain. J. Paleolimnol. 46, 487–502.

820 Goldberg, T., Archer, C., Vance, D., Thamdrup, B., McAnena, A., Poulton, S.W., 2012.
821 Controls on Mo isotope fractionations in a Mn-rich anoxic marine sediment,
822 Gullmar Fjord, Sweden. Chem. Geol. 296-297, 73–82.

823 Gomez-Parra, A., Establier, R., Escolar, D., 1984. Heavy metals in recent sediments
824 from the Bay of Cadiz, Spain. Mar. Pollut. Bull. 15, 1982–1985.

825 Gomez-Parra, A., Forja, J.M., 1992. Significance of benthic regeneration in nutrient
826 balance in the Bay of Cadiz, south-west Spain (a shallow semi-closed coastal
827 ecosystem). Sci. Total Environ. 1079–1086.

828 Gutiérrez-Mas, J.M., López-Aguayo, F., Achab, M., 2006. Clay minerals as dynamic
829 tracers of suspended matter dispersal in the Gulf of Cadiz (SW Spain). Clay Miner.
830 41, 727–738.

831 Gutiérrez-Mas, J.M., López-Arroyo, J., Morales, J.A., 2009. Recent marine lithofacies
832 in Cadiz Bay (SW Spain). Sediment. Geol. 218, 31–47.

833 Gutiérrez-Mas, J.M., Moral, J.P., Sánchez, A., Dominguez, S., Muñoz-Perez, J.J., 2003.
834 Multicycle sediments on the continental shelf of Cadiz (SW Spain). Estuar. Coast.
835 Shelf Sci. 57, 667–677.

836 Gutiérrez-Mas, J.M., Parrado Román, J.M., Moral Carcona, J.P., Sánchez Bellón, A.,
837 González Caballero, J.L., López-Aguayo, F., 1997. Distribución de facies recientes

838 en los fondos de la Bahía de Cádiz. Geogaceta 21.
839 Izquierdo, C., Usero, J., Gracia, I., 1997. Speciation of Heavy Metals in Sediments from
840 Salt Marshes on the Southern Atlantic Coast of Spain. Mar. Pollut. Bull. 34, 123–
841 128.
842 Johannessen, S.C., Macdonald, R.W., 2012. There is no 1954 in that core! Interpreting
843 sedimentation rates and contaminant trends in marine sediment cores. Mar. Pollut.
844 Bull. 64, 675–678.
845 Jorgensen, B.B., 1982. Mineralization of organic matter in the sea bed - the role of
846 sulphate reduction. Nature 296, 643–645.
847 Jorgensen, B.B., Kasten, S., 2006. Sulfur cycling and methane oxidation. In: Schulz,
848 H.D., Zabel, M. (Eds.), Marine Geochemistry. Springer-Verlag, Berlin, pp. 271–
849 209.
850 Kendall, C., Elliott, E.M., Wankel, S.D., 2007. Tracing anthropogenic inputs of nitrogen
851 to ecosystems. In: Michener, R.H., Lajtha, K. (Eds.), Stable Isotopes in Ecology
852 and Environmental Science. Blackwell Publishing, pp. 375– 449.
853 Kohzu, A., Imai, A., Ohkouchi, N., Fukushima, T., Kamiya, K., Komatsu, K., Tomioka,
854 N., Kawasaki, N., Miura, S., Satou, T., 2011. Direct evidence for the alteration of
855 13 C natural abundances during early diagenesis in Lake Kasumigaura, Japan.
856 Geochemistry, Geophys. Geosystems 12, Q10008.
857 Lalonde, K., Mucci, A., Ouellet, A., Gélinas, Y., 2012. Preservation of organic matter in
858 sediments promoted by iron. Nature 483, 198–200.
859 Lamb, A.L., Wilson, G.P., Leng, M.J., 2006. A review of coastal palaeoclimate and
860 relative sea-level reconstructions using δ13C and C/N ratios in organic material.
861 Earth-Science Rev. 75, 29–57.
862 Lami, A., Turner, S., Musazzi, S., Gerli, S., Guilizzoni, P., Rose, N.L., Yang, H., Wu,
863 G., Yang, R., 2010. Sedimentary evidence for recent increases in production in
864 Tibetan plateau lakes. Hydrobiologia 648, 175–187.
865 Lario, J., Zazo, C., Goy, J.L., Dabrio, C.J., Borja, F., Silva, P.G., Sierro, F., González,
866 A., Soler, V., Yll, E., 2002. Changes in sedimentation trends in SW Iberia
867 Holocene estuaries (Spain). Quat. Int. 93-94, 171–176.
868 Lehmann, M.F., Bernasconi, S.M., Barbieri, A., McKenzie, J.A., 2002. Preservation of
869 organic matter and alteration of its carbon and nitrogen isotope composition during
870 simulated and in situ early sedimentary diagenesis. Geochim. Cosmochim. Acta
871 66, 3573–3584.
872 Lepland, A., Andersen, T.J., Lepland, A., Peter, H., Arp, H., Alve, E., Breedveld, G.D.,
873 Rindby, A., 2010. Sedimentation and chronology of heavy metal pollution in Oslo

874 harbor , Norway. Mar. Pollut. Bull. 60, 1512–1522.
875 Ligero, R.A., Barrera, M., Casas-Ruiz, M., Sales, D., López-Aguayo, F., 2002. Dating
876 of marine sediments and time evolution of heavy metal concentrations in the Bay
877 of Cádiz, Spain. Environ. Pollut. 118, 97–108.
878 Ligero, R.A., Casas-Ruiz, M., Barrera, M., Barbero, L., Meléndez, M.J., 2010. An
879 alternative radiometric method for calculating the sedimentation rates: application
880 to an intertidal region (SW of Spain). Appl. Radiat. Isot. 68, 1602–9.
881 Ligero, R.A., Casas-Ruiz, M., Barrera, M., López-Aguayo, F., Sales, D., García, D.,
882 2004. Environmental impact of unleaded gasolines in the bay of Cádiz (Spain).
883 Environ. Int. 30, 99–104.
884 Lovley, D.R., Stolz, J.F., Nord, G.L., Phillips, E.J.P., 1987. Anaerobic production of
885 magnetite by a dissimilatory iron-reducing microorganism. Nature 330, 252–254.
886 Macko, S.A., Estep, M.L.F., 1984. Microbial alteration of stable nitrogen and carbon
887 isotopic compositions of organic matter. Org. Geochem. 6, 787–790.
888 Martin, P., Handcock, G., 2004. Routine analysis of naturally occurring radionucleides
889 in environmental samples by alpha-particle spectrometry. Superv. Sci. Rep. 180,
890 Superv. Sci. Darwin NT.
891 Martinez-Ruiz, F., Koster, M., Gallego-Torres, D., Rodrigo-Gámiz, M., Nieto-Moreno,
892 V., Ortega-Huertas, M., 2015. Paleoclimate and paleoceanography over the past 20
893 , 000 yr in the Mediterranean Sea Basins as indicated by sediment elemental
894 proxies. Quat. Sci. Rev. 107, 25–46.
895 Martín-Puertas, C., Valero-Garcés, B.L., Mata, M.P., Moreno, A., Giralt, S., Martínez-
896 Ruiz, F., Jiménez-Espejo, F., 2009. Geochemical processes in a Mediterranean
897 Lake: a high-resolution study of the last 4,000 years in Zoñar Lake, southern
898 Spain. J. Paleolimnol. 46, 405–421.
899 Meyers, P.A., 1994. Preservation of elemental and isotopic source identification of
900 sedimentary organic matter. Chem. Geol. 114, 289–302.
901 Meyers, P.A., 1997. Organic geochemical proxies of paleoceanographic,
902 paleolimnologic, and paleoclimatic processes. Org. Geochem. 27, 213–1997.
903 Middelburg, J.J., Vlug, T., van der Nat, F.J.W.A., 1993. Organic matter mineralization
904 in marine systems. Glob. Planet. Change 8, 47–58.
905 Möbius, J., 2013. Isotope fractionation during nitrogen remineralization
906 (ammonification): Implications for nitrogen isotope biogeochemistry. Geochim.
907 Cosmochim. Acta 105, 422–432.
908 Montoya, J.P., 2007. Natural abundance of 15N in marine planktonic ecosystems. In:

909 Michener, R.H., Lajtha, K. (Eds.), Stable Isotopes in Ecology and Environmental
910 Science. Blackwell Publishing, pp. 176–201.
911 Morillo, J., Usero, J., Gracia, I., 2007. Potential Mobility of Metals in Polluted Coastal
912 Sediments in Two Bays of Southern Spain. J. Coast. Res. 232, 352–361.
913 Morris, E.P., Peralta, G., Benavente, J., Freitas, R., Rodrigues, A.M., Quintino, V.,
914 Alvarez, O., Valcárcel-Pérez, N., Vergara, J.J., Hernández, I., Pérez-Lloréns, J.L.,
915 2009. Caulerpa prolifera stable isotope ratios reveal anthropogenic nutrients within
916 a tidal lagoon. Mar. Ecol. Prog. Ser. 390, 117–128.
917 Mucci, A., Boudreau, B., Guignard, C., 2003. Diagenetic mobility of trace elements in
918 sediments covered by a flash flood deposit: Mn, Fe and As. Appl. Geochemistry
919 18, 1011–1026.
920 Mucci, A., Edenborn, H.M., 1992. Influence of an organic-poor landslide deposit on the
921 early diagenesis of iron and manganese in a coastal marine sediment. Geochim.
922 Cosmochim. Acta 56, 3909–3921.
923 Müller, P.J., 1977. C/N ratios in Pacific deep-sea sediments: Effect of inorganic
924 ammonium and organic nitrogen compounds sorbed by clays. Geochim.
925 Cosmochim. Acta 41.
926 Muñoz Perez, J.L., Sánchez de LaMadrid Rey, A., 1994. El medio fisico y biologico en
927 la Bahia de Cadiz: Saco interior. Centro de Investigación y Cultivo de Especies
928 Marinas “El Toruño.”
929 Ponce, R., Forja, J.M., Gómez-Parra, A., 2000. Influence of anthropogenic activity on
930 the vertical distribution of Zn, Cd, Pb and Cu in intersticial water and coastal
931 marine sediments (Cadiz Bay, SW Spain). Ciencias Mar. 26, 479–502.
932 Ponce, R., Ortega, T., Forja, J.M., 2010. Accumulation of phosphorus in coastal marine
933 sediments : relationship to benthic and diffusive fluxes. Sci. Mar. 115–124.
934 Poulton, S.W., Canfield, D.E., 2005. Development of a sequential extraction procedure
935 for iron: implications for iron partitioning in continentally derived particulates.
936 Chem. Geol. 214, 209–221.
937 Poulton, S.W., Fralick, P.W., Canfield, D.E., 2004a. The transition to a sulphidic ocean
938 ~1.84 billion years ago. Nature 431, 173–177.
939 Poulton, S.W., Krom, M.D., Raiswell, R., 2004b. A revised scheme for the reactivity of
940 iron (oxyhydr)oxide minerals towards dissolved sulfide. Geochim. Cosmochim.
941 Acta 68, 3703–3715.
942 Raiswell, R., Canfield, D.E., 1998. Sources of iron for pyrite formation in marine
943 sediments. Am. J. Sci. 298, 219–245.

944 Ridgway, J., Andrews, J.E., Ellis, S., Horton, B.P., Innes, J.B., Knox, R.W.O.,
945 McArthur, J.J., Maher, B.A., Metcalfe, S.E., Mitlehner, A., Parkes, A., Rees, J.G.,
946 Samways, G.M., Shennan, I., 2000. Analysis and interpretation of Holocene
947 sedimentary sequences in the Humber Estuary. Geol. Soc. London, Spec. Publ.
948 166 , 9–39.

949 Ridgway, J., Shimmield, G., 2002. Estuaries as Repositories of Historical
950 Contamination and their Impact on Shelf Seas. Estuar. Coast. Shelf Sci. 55, 903–
951 928.

952 Robinson, R.S., Kienast, M., Luiza Albuquerque, A., Altabet, M., Contreras, S., De Pol
953 Holz, R., Dubois, N., Francois, R., Galbraith, E., Hsu, T.-C., Ivanochko, T.,
954 Jaccard, S., Kao, S.-J., Kiefer, T., Kienast, S., Lehmann, M., Martinez, P.,
955 McCarthy, M., Möbius, J., Pedersen, T., Quan, T.M., Ryabenko, E., Schmittner,
956 A., Schneider, R., Schneider-Mor, A., Shigemitsu, M., Sinclair, D., 2012. A review
957 of nitrogen isotopic alteration in marine sediments. Paleoceanography 27, 1944–
958 9186.

959 Rothwell, R.G., Hoogakker, B., Thomson, J., Croudace, I.W., Frenz, M., 2006.
960 Turbidite emplacement on the southern Balearic Abyssal Plain (western
961 Mediterranean Sea) during Marine Isotope Stages 1–3: an application of ITRAX
962 XRF scanning of sediment cores to lithostratigraphic analysis. Geol. Soc. London,
963 Spec. Publ. 267, 79–98.

964 Ruttenberg, K.C., Berner, R.A., 1993. Authigenic apatite formation and burial in
965 sediments from non-upwelling, continental margin environments. Geochim.
966 Cosmochim. Acta 57, 991–1007.

967 Sáenz, V., Blasco, J., Gómez-Parra, A., 2003. Speciation of heavy metals in recent
968 sediments of three coastal ecosystems in the Gulf of Cádiz, Southwest Iberian
969 Peninsula. Environ. Toxicol. Chem. 22, 2833–2839.

970 Sageman, B.B., Lyons, T.W., 2005. Geochemistry of Fine-grained Sediments and
971 Sedimentary Rocks. In: Holland, H.D., Turekian, K.K. (Eds.), Treatise on
972 Geochemistry. Elsevier-Pergamon, pp. 115–158.

973 Slomp, C.P., Epping, E.H.G., Helder, W., Raaphorst, W. Van, 1996. A key role for
974 iron-bound phosphorus in authigenic apatite formation in North Atlantic
975 continental platform sediments. J. Mar. Res. 54, 1179–1205.

976 Spencer, K.L., Cundy, A.B., Croudace, I.W., 2003. Heavy metal distribution and early-
977 diagenesis in salt marsh sediments from the Medway Estuary, Kent, UK. Estuar.
978 Coast. Shelf Sci. 57, 43–54.

979 Syvitski, J.P.M., Milliman, J.D., 2007. Geology , Geography , and Humans Battle for
980 Dominance over the Delivery of Fluvial Sediment to the Coastal Ocean. J. Geol.

115, 1–19.

Syvitski, J.P.M., Vörösmarty, C.J., Kettner, A.J., Green, P., 2005. Impact of humans on the flux of terrestrial sediment to the global coastal ocean. Science 308, 376–80.

Thomson, J., Croudace, I.W., Rothwell, R.G., 2006. A geochemical application of the ITRAX scanner to a sediment core containing eastern Mediterranean sapropel units. Geol. Soc. London, Spec. Publ. 267, 65–77.

Tjallingii, R., Röhl, U., Kölling, M., Bickert, T., 2007. Influence of the water content on X-ray fluorescence core-scanning measurements in soft marine sediments. Geochemistry, Geophys. Geosystems 8, 1–12.

Tribovillard, N., Algeo, T.J., Lyons, T., Riboulleau, A., 2006. Trace metals as paleoredox and paleoproductivity proxies: An update. Chem. Geol. 232, 12–32.

Voss, M., Larsen, B., Leivuori, M., Vallius, H., 2000. Stable isotope signals of eutrophication in Baltic Sea sediments. J. Mar. Syst. 25, 287–298.

Wigand, C., Mckinney, R.A., Cole, M.L., Thursby, G.B., Cummings, J., 2007. Varying Stable Nitrogen Isotope Ratios of Different Coastal Marsh Plants and Their Relationships with Wastewater Nitrogen and Land Use in New England , USA. Environ. Monit. Assess. 71–81.

Zegeye, A., Bonneville, S., Benning, L.G., Sturm, A., Fowle, D.A., Jones, C., Canfield, D.E., Ruby, C., MacLean, L.C., Nomosatryo, S., Crowe, S.A., Poulton, S.W., 2012. Green rust formation controls nutrient availability in a ferruginous water column. Geology 40, 599–602.

Zimmerman, A.R., Canuel, E.A., 2000. A geochemical record of eutrophication and anoxia in Chesapeake Bay sediments: anthropogenic influence on organic matter composition. Mar. Chem. 69, 117–137.

Figures captions

Figure 1. Map of Cádiz Bay area showing the locations of sampling sites (Z1, Z2 and Z3). Circles correspond to the position of cores in September 2009 and triangles of cores in April 2011 (detailed information about these samples is given in Table1)

Figure 2. Stratigraphic diagram showing the main lithological features for Z1, Z2 and Z3 (from top to bottom). Vertical profiles of selected elemental ratios from the XRF core-scanner and the proportion of fine grained sediment obtained from the mineralogical data are shown for the same cores. Dashed horizontal lines indicate the division among stratigraphic units (H1, H2 and H3) for each sampling site.

Figure 3. Al-normalized depth profiles for Fe, Mn, P, V, Cu and Zn for Z1 and Z2. The onset of unit H2 is 70 and 30 cm depth for Z1 and Z2, respectively

Figure 4. Depth profile of XRF core scanner for Z1 (a) and Z2 (b). The dashed line indicates the onset of H2. Note the area shaded in grey indicates an artefact (lost signal due to the fact that surface of sediment was not even)

Figure 5. Depth profiles of chemical partitioning of Fe at Z1 (upper panels) and Z2 (lower panels). The onset of unit H2 is 70 and 30 cm depth for Z1 and Z2, respectively

Figure 6. Depth profiles of Corg, carbonates and molar Corg/N ratio for Z1 and Z2. The onset of unit H2 is 70 and 30 cm depth for Z1 and Z2, respectively

Figure 7. Depth profile for δ13C and δ15N stable isotopes at sampling sites Z1 and Z2. The onset of unit H2 is 70 and 30 cm depth for Z1 and Z2, respectively

Figure 8. Evolution of sediment accumulation rates at sampling sites Z1 and Z2. Grey shaded area indicates the mixed layer (see section 3.6). Note that years correspond to approximated ages.

Figure 9. Summary diagram of the major environmental changes in the inner Cadiz Bay. Information on the number of inhabitants was obtained from census data gathered by the Spanish National Statistical Institute (INE).The calculation includes all of the municipalities that belong to Cadiz Bay from an administrative point of view, and/or that drain sewage into the watershed of the Guadalete, Salado and Iro rivers (Cádiz, Chiclana de la Frontera, Puerto de Santa Maria, Puerto Real, Rota, San Fernando, Jerez

de la Frontera and San Jose del Valle). Grey shaded area indicates the mixed layer (see section 3.6). Note that years correspond to approximated ages.

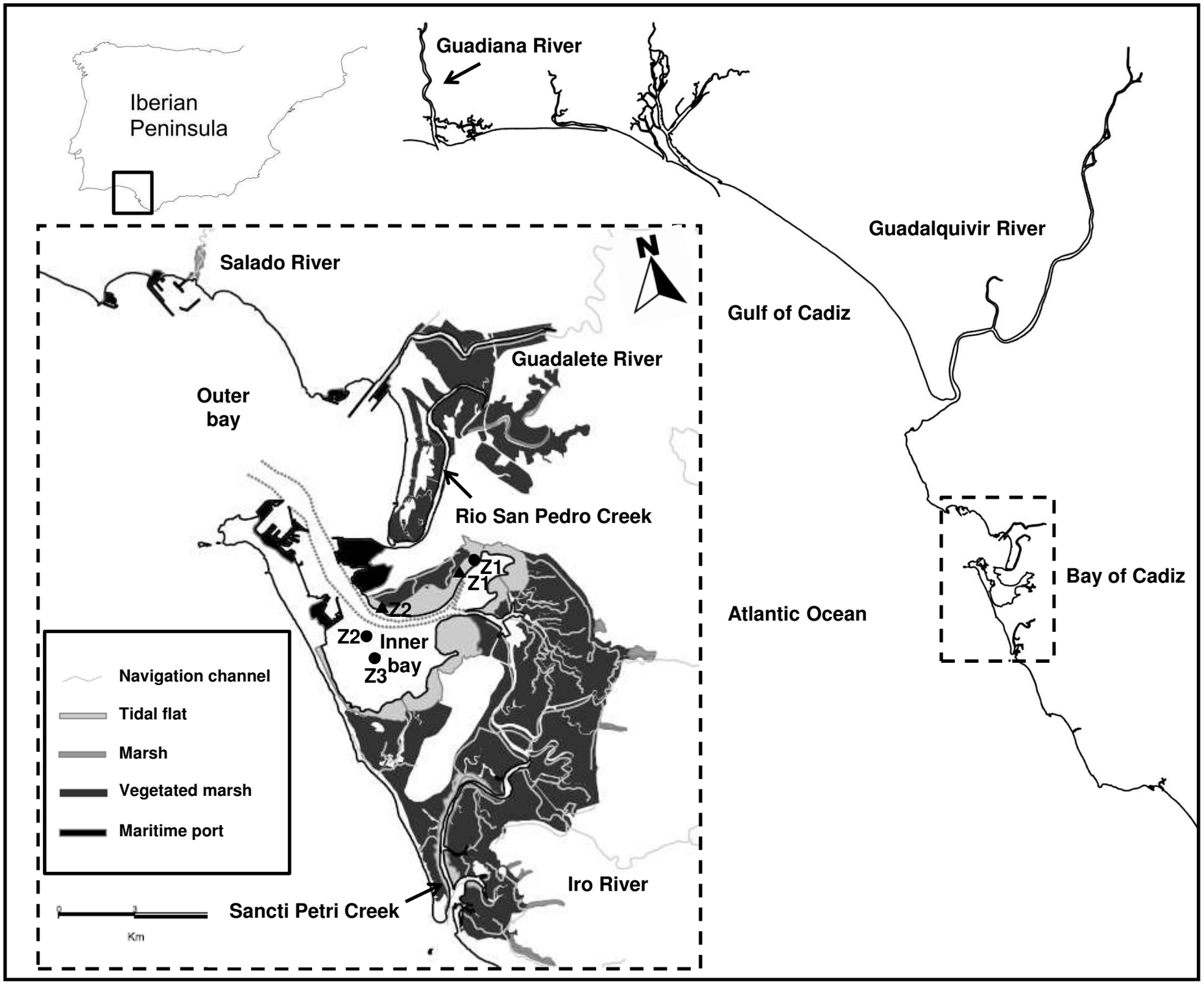
Iberian
Peninsula
Guadiana River
Guadalquivir River
Gulf of Cadiz
Atlantic Ocean
Bay of Cadiz
Salado River
Guadalete River
Outer
bay
Rio San Pedro Creek
Z1
Z1
Z2
Z2
Inner
bay
Z3
Iro River
Sancti Petri Creek
N
Navigation channel
Tidal flat
Marsh
Vegetated marsh
Maritime port
0
3
Km

Figure 1

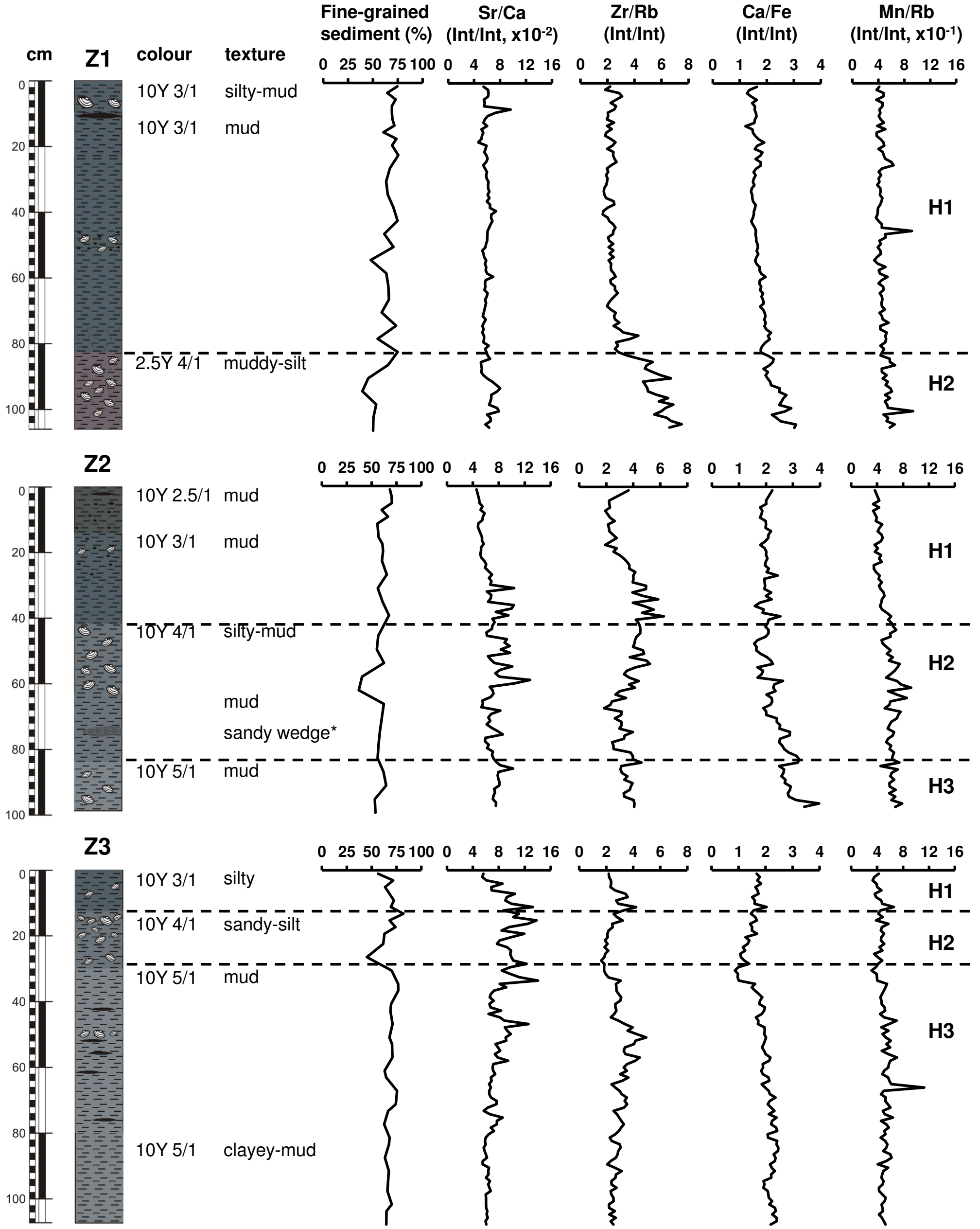
cm
Z1
colour
texture
Fine-grained sediment (%)
Sr/Ca (Int/Int, x10-2)
Zr/Rb (Int/Int)
Ca/Fe (Int/Int)
Mn/Rb (Int/Int, x10-1)
0 25 50 75 100
0 4 8 12 16
0 2 4 6 8
0 1 2 3 4
0 4 8 12 16
0
20
40
60
80
100
10Y 3/1 silty-mud
10Y 3/1 mud
2.5Y 4/1 muddy-silt
H1
H2
Z2
10Y 2.5/1 mud
10Y 3/1 mud
10Y 4/1 silty-mud
mud
sandy wedge*
10Y 5/1 mud
H1
H2
H3
Z3
10Y 3/1 silty
10Y 4/1 sandy-silt
10Y 5/1 mud
10Y 5/1 clayey-mud
H1
H2
H3

Figure 2

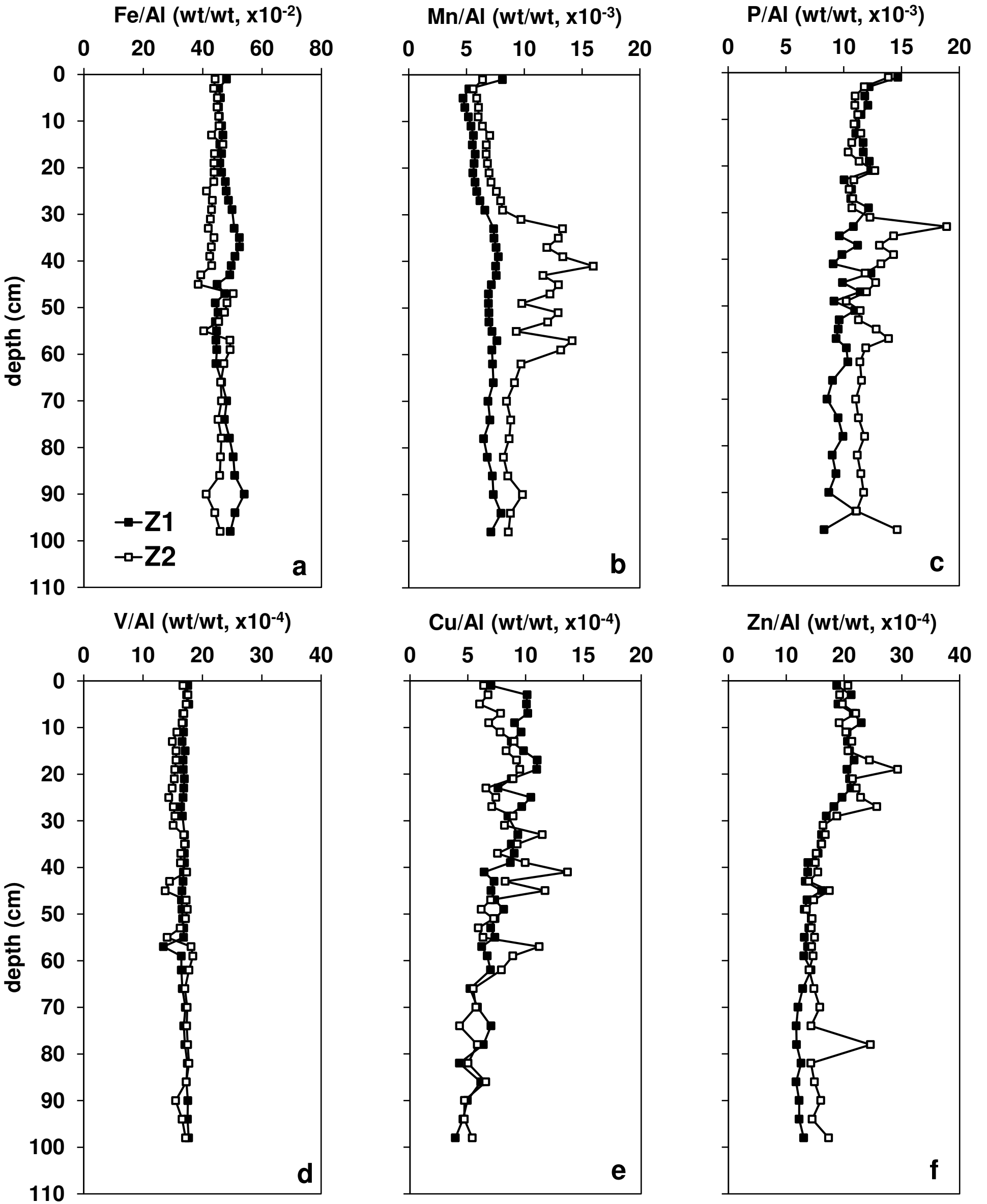
Fe/Al (wt/wt, x10-2)
Mn/Al (wt/wt, x10-3)
P/Al (wt/wt, x10-3)
V/Al (wt/wt, x10-4)
Cu/Al (wt/wt, x10-4)
Zn/Al (wt/wt, x10-4)
depth (cm)
Z1
Z2
a
b
c
d
e
f

Figure 3

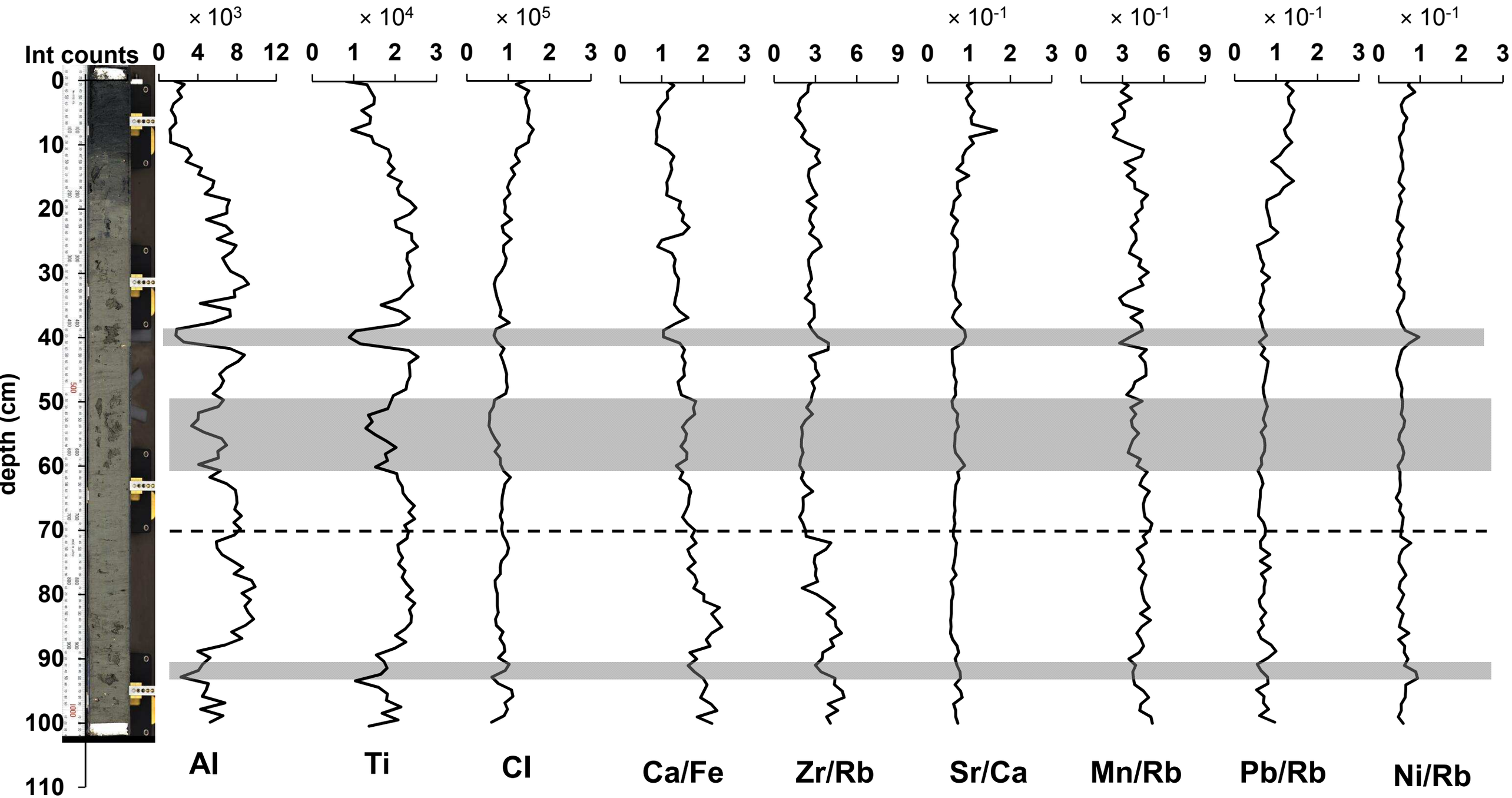
Int counts
× 10^3
× 10^4
× 10^5
× 10^-1
× 10^-1
× 10^-1
× 10^-1
0 4 8 12
0 1 2 3
0 1 2 3
0 1 2 3
0 3 6 9
0 1 2 3
0 3 6 9
0 1 2 3
0 1 2 3
depth (cm)
0
10
20
30
40
50
60
70
80
90
100
110
Al
Ti
Cl
Ca/Fe
Zr/Rb
Sr/Ca
Mn/Rb
Pb/Rb
Ni/Rb

Figure 4a

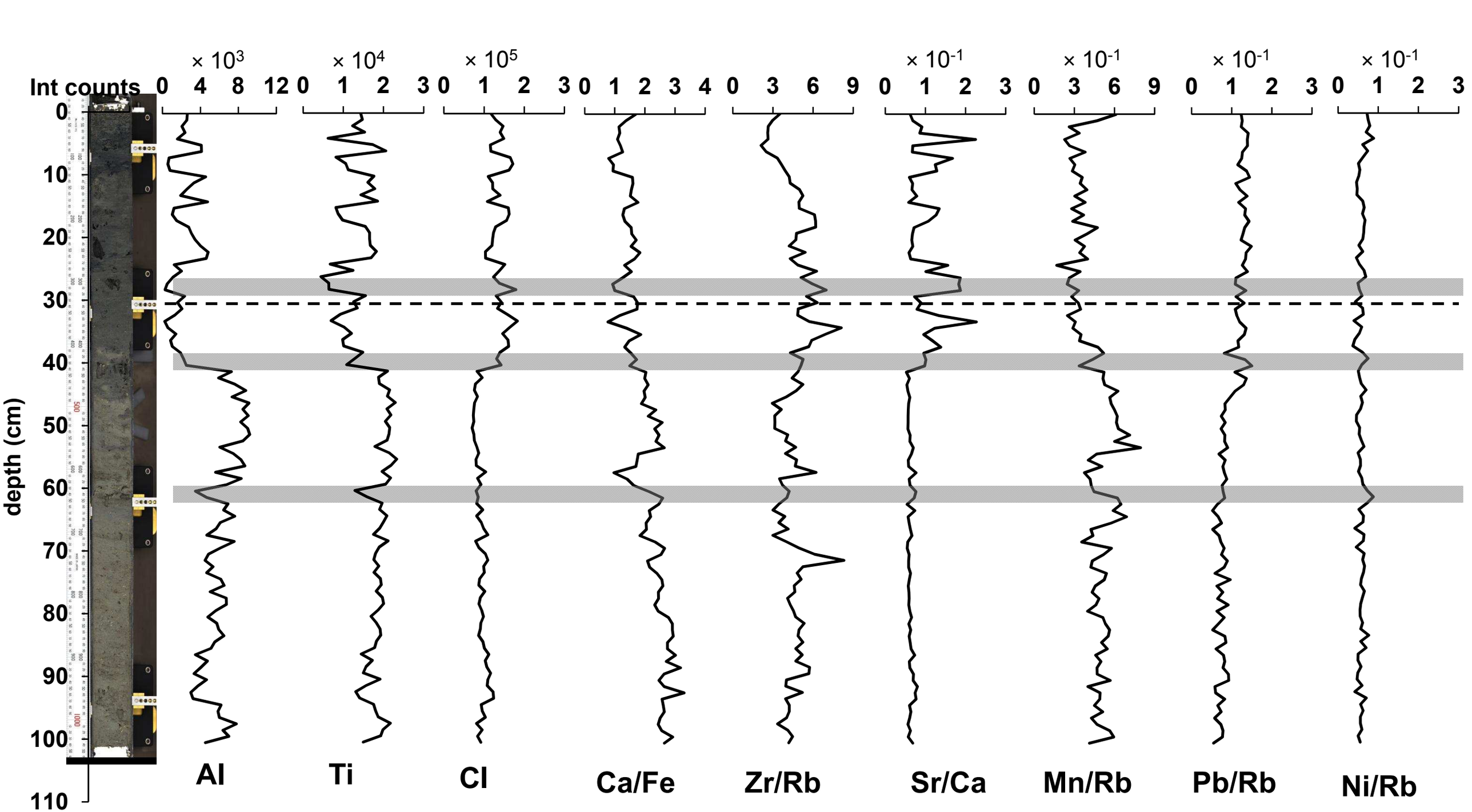
Int counts
× 10³
0 4 8 12
× 10⁴
0 1 2 3
× 10⁵
0 1 2 3
0 1 2 3 4
0 3 6 9
× 10⁻¹
0 1 2 3
× 10⁻¹
0 3 6 9
× 10⁻¹
0 1 2 3
× 10⁻¹
0 1 2 3
depth (cm)
0
10
20
30
40
50
60
70
80
90
100
110
Al
Ti
Cl
Ca/Fe
Zr/Rb
Sr/Ca
Mn/Rb
Pb/Rb
Ni/Rb

Figure 4b

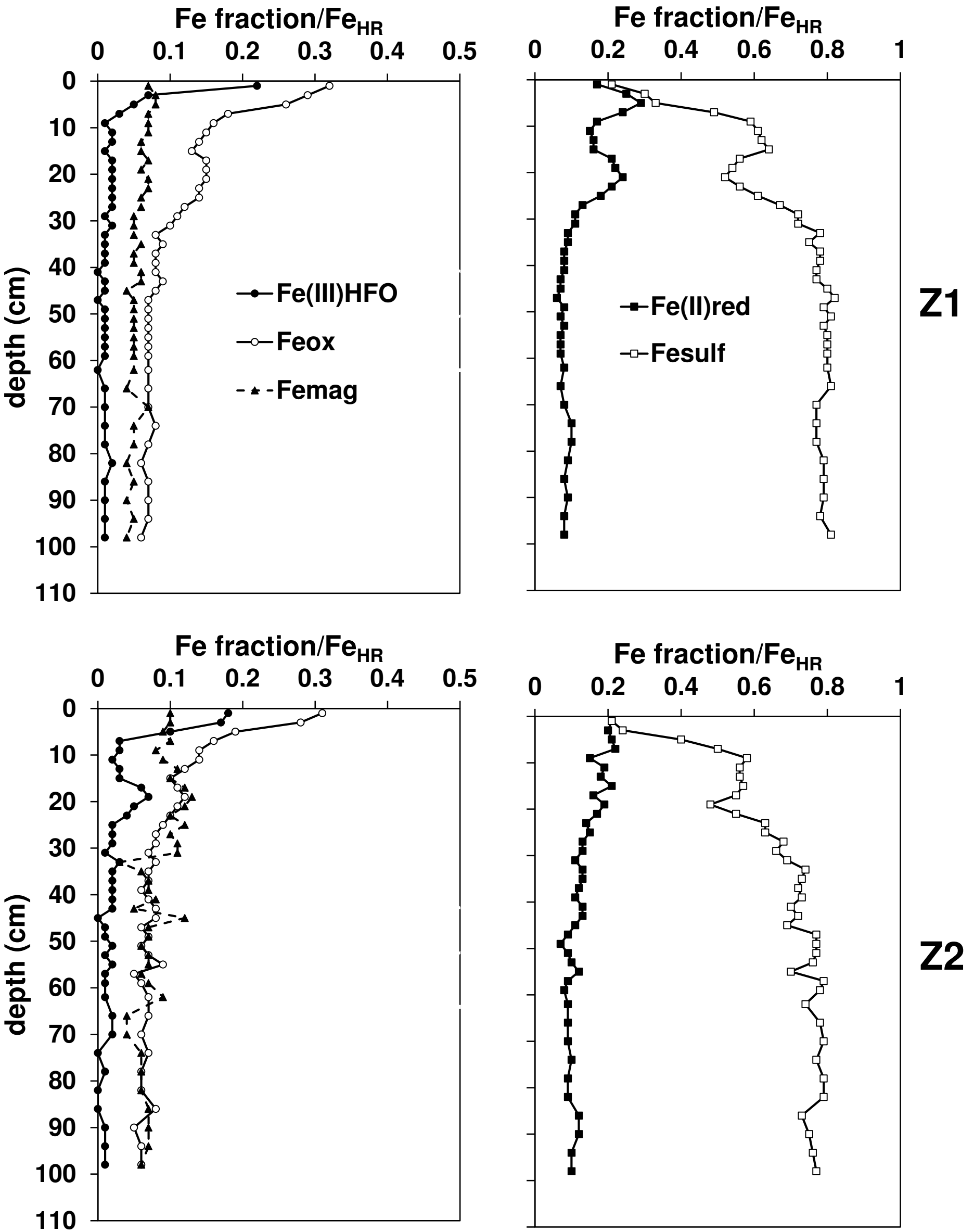
Fe fraction/Fe$_{HR}$
0
0.1
0.2
0.3
0.4
0.5
0.6
0.8
1
depth (cm)
10
20
30
40
50
60
70
80
90
100
110
Fe(III)HFO
Feox
Femag
Fe(II)red
Fesulf
Z1
Z2

Figure 5

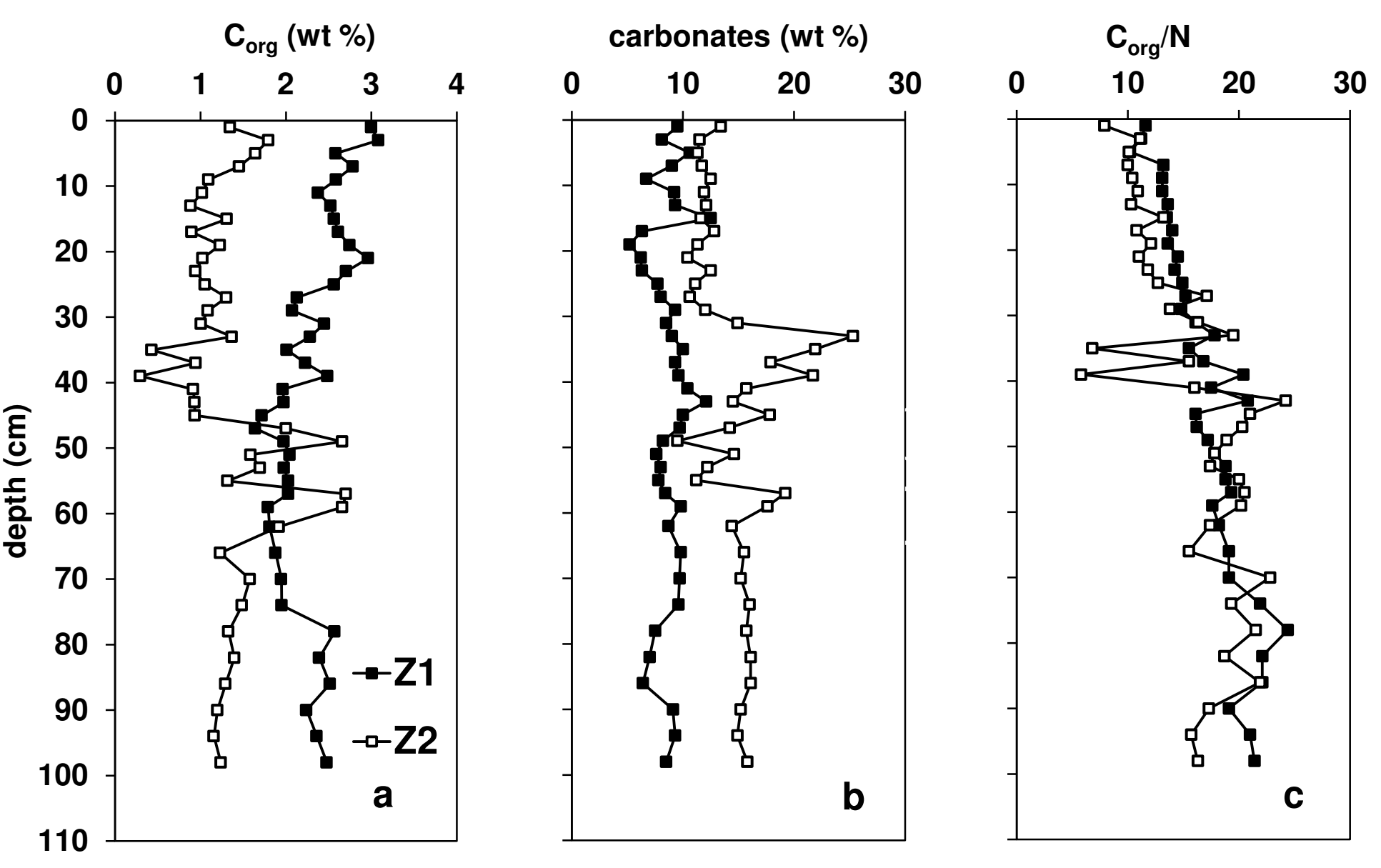
C_org (wt %)
0
1
2
3
4
carbonates (wt %)
0
10
20
30
C_org/N
0
10
20
30
depth (cm)
0
10
20
30
40
50
60
70
80
90
100
110
Z1
Z2
a
b
c

Figure 6

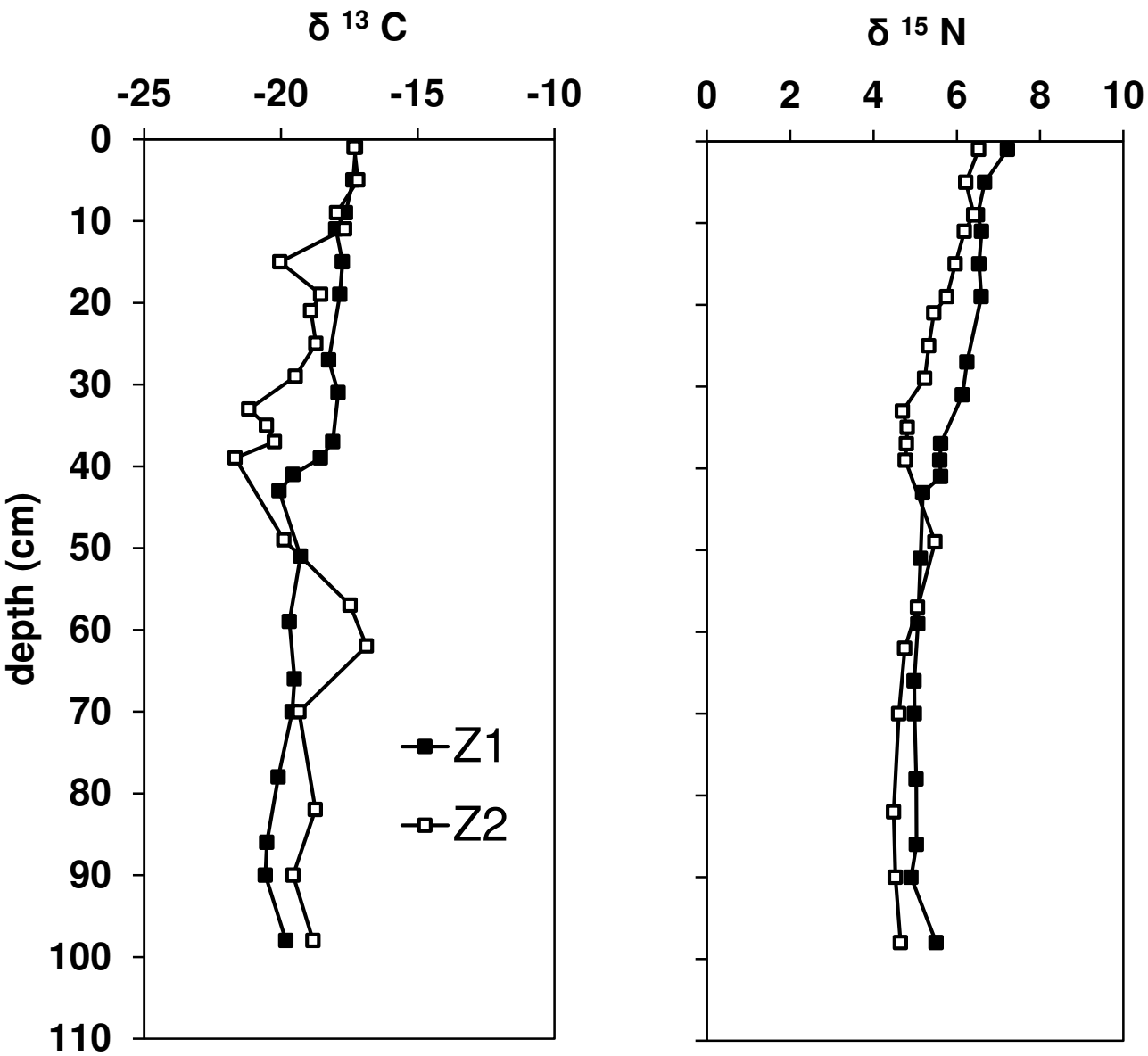
δ 13 C
-25
-20
-15
-10
δ 15 N
0
2
4
6
8
10
depth (cm)
0
10
20
30
40
50
60
70
80
90
100
110
Z1
Z2

Figure 7

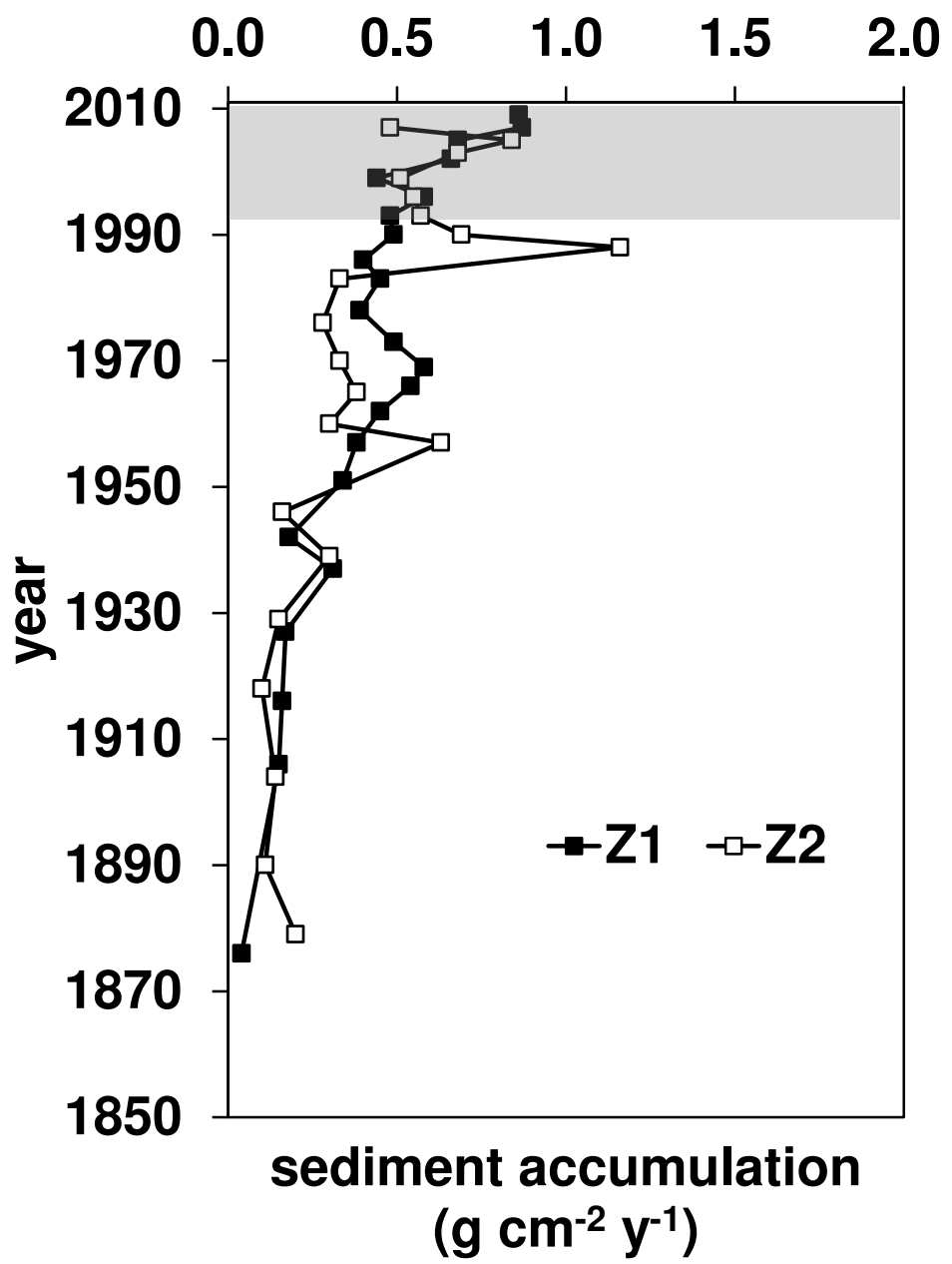
0.0
0.5
1.0
1.5
2.0
2010
1990
1970
1950
1930
1910
1890
1870
1850
year
Z1
Z2
sediment accumulation
(g cm-2 y-1)

Figure 8

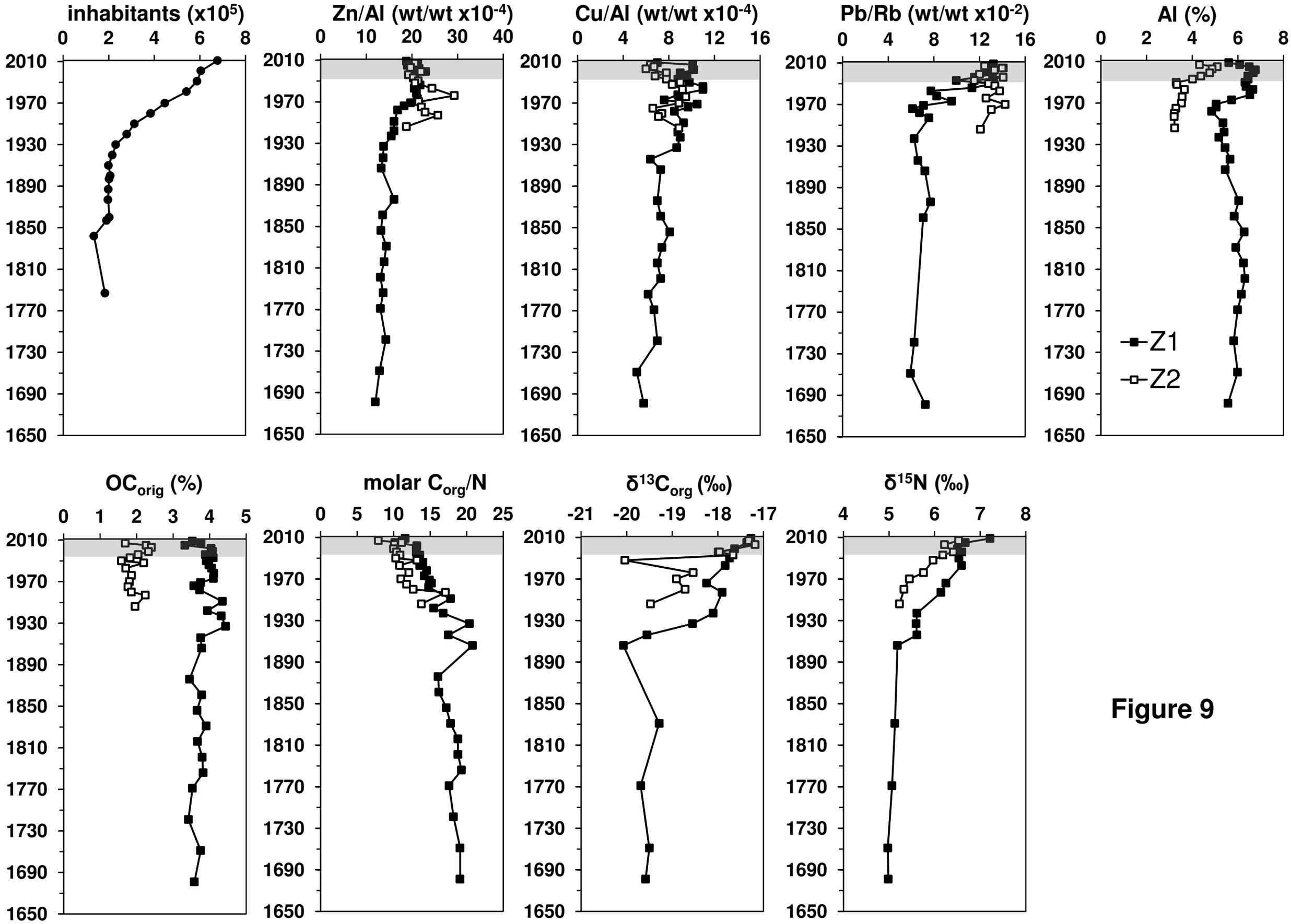
inhabitants (x10^5)
0 2 4 6 8
Zn/Al (wt/wt x10^-4)
0 10 20 30 40
Cu/Al (wt/wt x10^-4)
0 4 8 12 16
Pb/Rb (wt/wt x10^-2)
0 4 8 12 16
Al (%)
0 2 4 6 8
2010
1970
1930
1890
1850
1810
1770
1730
1690
1650
Z1
Z2
OC_orig (%)
0 1 2 3 4 5
molar C_org/N
0 5 10 15 20 25
δ13C_org (‰)
-21 -20 -19 -18 -17
δ15N (‰)
4 5 6 7 8

Figure 9

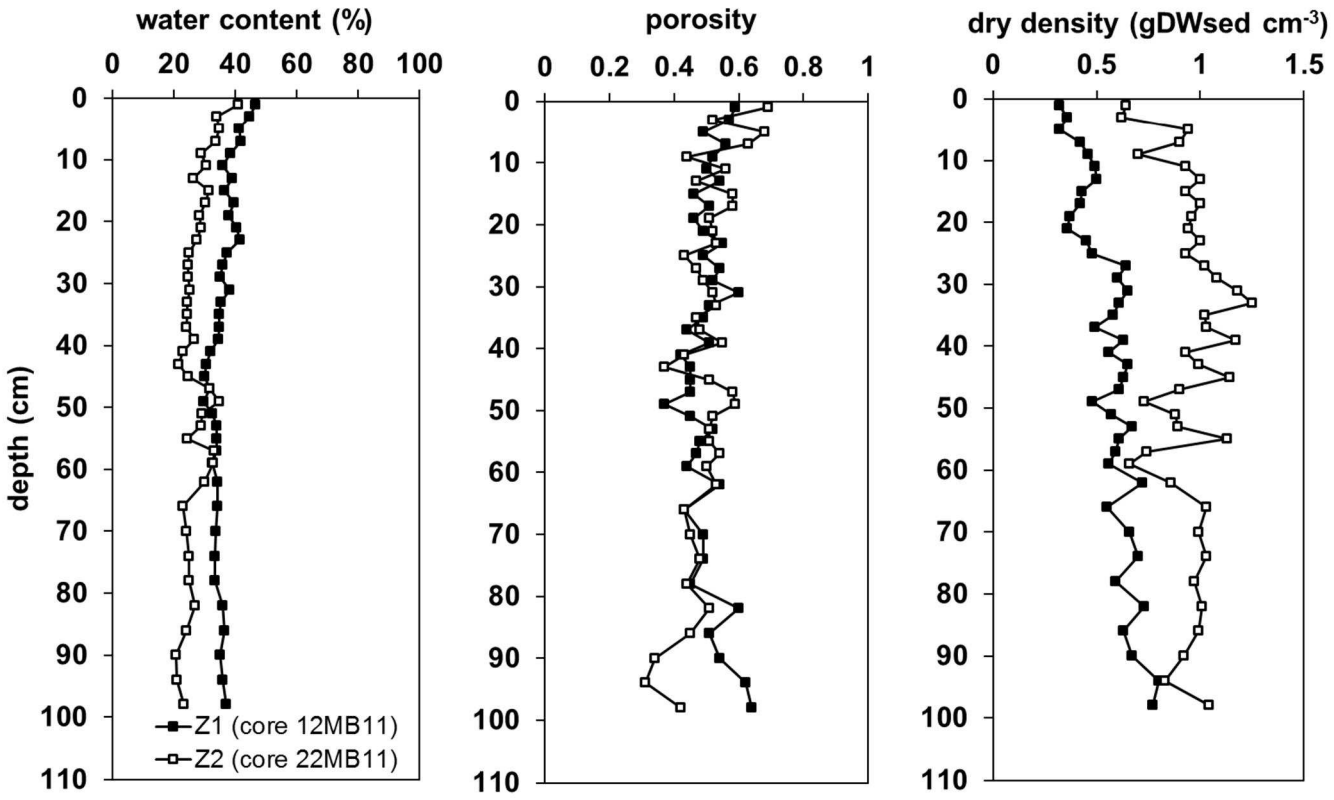

Fig S1. Depth profiles of water content, porosity, and dry density of sediment for stations Z1 and Z2.

Equations:

Water content (%) = $100 \times (gWW_{sed} - gDW_{sed}) / gWW_{sed}$

Dry density (gDW_{sed} cm^{-3}) = gDW_{sed} / V

Porosity (vol:vol) = V_f/V

where :

gWW_{sed} and gDW_{sed} are the sediment weights (g) before and after of freeze-drying

V is the volume of each sample slice (cm^3)

V_f is the volume of pore space (cm^3) determined using the weight loss of water after freeze-drying (g) and the sea water density (1.024 gr cm^{-3}).

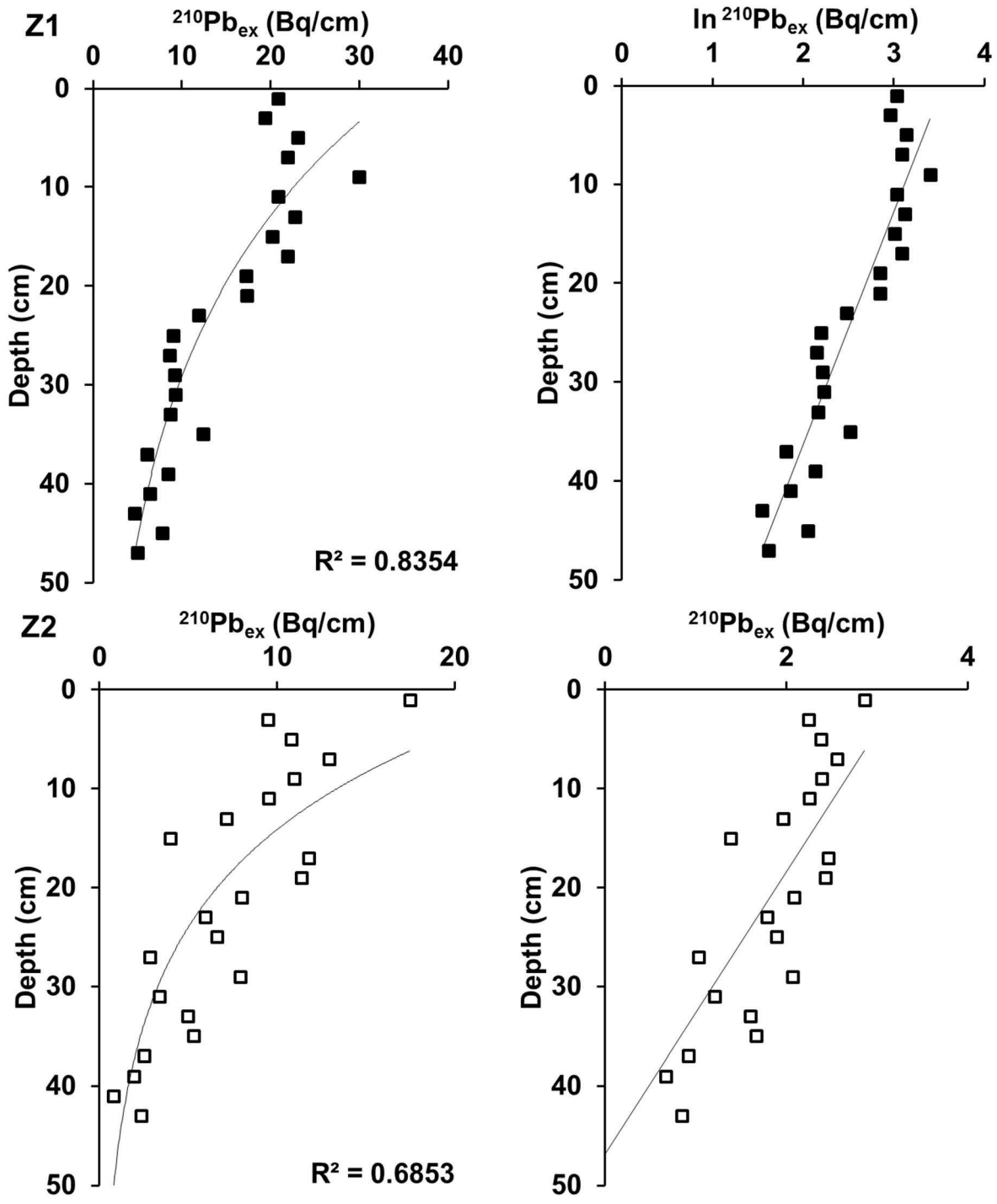

Fig S2. Depth profiles of Excess Pb-210 activity and its natural log for stations Z1 and Z2.

Table S1. Concentrations of total and excess 210-Pb, 226-Ra activity, sedimentation rates (v), sediment accumulation rates (r), and approximate ages of each slice for stations Z1 and Z2. Numbers to the right of plus-minus symbol denote the experimental error in the determination of 210-Pb and 226-Ra activity and the propagated error coming from counting statistics. LOD: limit of detection. Numbers in parenthesis indicates the dating error arising from CRS model. Asterisk indicates the approximate age of the top slice.

Z1						
Depth (cm)	**$^{210}Pb_{total}$ (Bq/kg)**	**^{226}Ra (Bq/kg)**	**$^{210}Pb_{ex}$ (Bq/kg)**	**v (cm/y)**	**r (g/cm^2y)**	**Age (years AD)**
1	29.6 ± 0.44	<LOD	-	-	-	-
3	29.7 ± 0.44	8.90 ± 2.58	20.8 ± 0.29	1.04 ± 0.09	0.86 ± 0.07	2009 (0)*
5	29.4 ± 0.43	10.1 ± 2.39	19.3 ± 0.24	1.04 ± 0.10	0.87 ± 0.08	2007 (0)
7	29.7 ± 0.44	6.68 ± 2.06	23.1 ± 0.31	0.75 ± 0.07	0.68 ± 0.06	2005 (0)
9	32.1 ± 0.47	10.1 ± 2.45	21.9 ± 0.24	0.80 ± 0.08	0.66 ± 0.06	2002 (0)
11	36.3 ± 0.53	6.34 ± 2.61	30.0 ± 0.41	0.62 ± 0.06	0.44 ± 0.04	1999 (0)
13	25.7 ± 0.38	4.88 ± 2.04	20.8 ± 0.42	0.68 ± 0.06	0.58 ± 0.05	1996 (1)
15	29.8 ± 0.45	6.99 ± 2.23	22.8 ± 0.32	0.58 ± 0.06	0.48 ± 0.05	1993 (1)
17	31.3 ± 0.46	11.0 ± 2.37	20.2 ± 0.22	0.59 ± 0.06	0.49 ± 0.05	1990 (1)
19	28.7 ± 0.42	6.84 ± 2.01	21.9 ± 0.29	0.45 ± 0.05	0.40 ± 0.04	1986 (1)
21	25.1 ± 0.37	7.85 ± 1.95	17.2 ± 0.25	0.58 ± 0.07	0.45 ± 0.05	1983 (1)
23	26.7 ± 0.39	9.43 ± 1.88	17.3 ± 0.20	0.38 ± 0.04	0.39 ± 0.04	1978 (1)
25	20.9 ± 0.31	8.94 ± 1.64	11.9 ± 0.18	0.40 ± 0.04	0.49 ± 0.05	1973 (1)
27	19.7 ± 0.29	10.7 ± 1.85	9.00 ± 0.17	0.53 ± 0.06	0.58 ± 0.06	1969 (1)
29	19.9 ± 0.29	11.3 ± 2.03	8.58 ± 0.18	0.53 ± 0.06	0.54 ± 0.06	1966 (1)
31	20.7 ± 0.31	11.6 ± 1.88	9.16 ± 0.16	0.43 ± 0.05	0.45 ± 0.05	1962 (1)
33	19.5 ± 0.29	10.2 ± 2.03	9.31 ± 0.20	0.39 ± 0.04	0.38 ± 0.04	1957 (1)
35	18.5 ± 0.27	9.77 ± 1.95	8.72 ± 0.20	0.32 ± 0.04	0.34 ± 0.04	1951 (1)
37	19.6 ± 0.29	7.22 ± 1.69	12.4 ± 0.23	0.19 ± 0.02	0.18 ± 0.02	1942 (1)
39	17.4 ± 0.26	11.3 ± 2.16	6.10 ± 0.19	0.37 ± 0.05	0.31 ± 0.04	1937 (2)
41	19.15 ± 0.28	10.7 ± 1.88	8.45 ± 0.18	0.17 ± 0.02	0.17 ± 0.02	1927 (2)
43	18.67 ± 0.27	12.2 ± 1.98	6.43 ± 0.16	0.16 ± 0.02	0.16 ± 0.02	1916 (2)
45	17.68 ± 0.26	13.0 ± 2.06	4.69 ± 0.16	0.16 ± 0.02	0.15 ± 0.02	1906 (3)
47	20.15 ± 0.30	12.35 ± 1.99	7.80 ± 0.16	0.04 ± 0.01	0.04 ± 0.01	1876 (4)
49	16.49 ± 0.24	11.46 ± 1.97	5.03 ± 0.17	-	-	-

Z2						
Depth (cm)	**$^{210}Pb_{total}$ (Bq/kg)**	**^{226}Ra (Bq/kg)**	**$^{210}Pb_{ex}$ (Bq/kg)**	**v (cm/y)**	**r (g/cm^2y)**	**Age (years AD)**
1	23.1 ± 0.34	5.58 ± 1.94	17.5 ± 0.35	0.53 ± 0.10	0.48 ± 0.09	2007 (1)*
3	20.8 ± 0.31	11.4 ± 2.41	9.48 ± 0.21	1.00 ± 0.20	0.84 ± 0.17	2005 (1)
5	21.6 ± 0.32	10.8 ± 2.22	10.8 ± 0.21	0.74 ± 0.14	0.68 ± 0.13	2003 (1)
7	22.9 ± 0.34	9.94 ± 2.04	12.9 ± 0.21	0.56 ± 0.11	0.51 ± 0.10	1999 (1)
9	21.6 ± 0.32	10.7 ± 2.14	11.0 ± 0.20	0.61 ± 0.12	0.55 ± 0.11	1996 (1)
11	19.7 ± 0.30	10.2 ± 1.90	9.53 ± 0.19	0.60 ± 0.13	0.57 ± 0.12	1993 (1)
13	18.5 ± 0.27	11.4 ± 1.77	7.13 ± 0.16	0.57 ± 0.12	0.69 ± 0.14	1990 (1)
15	14.6 ± 0.22	10.6 ± 1.69	4.00 ± 0.16	1.17 ± 0.24	1.16 ± 0.24	1988 (1)
17	21.4 ± 0.32	9.57 ± 1.62	11.8 ± 0.17	0.34 ± 0.07	0.33 ± 0.07	1983 (1)
19	20.0 ± 0.30	8.64 ± 1.65	11.4 ± 0.19	0.28 ± 0.06	0.28 ± 0.06	1976 (1)
21	19.8 ± 0.29	11.8 ± 1.89	8.03 ± 0.16	0.30 ± 0.06	0.33 ± 0.07	1970 (1)
23	18.0 ± 0.27	12.1 ± 1.84	5.96 ± 0.15	0.39 ± 0.08	0.38 ± 0.08	1965 (1)
25	18.0 ± 0.27	11.4 ± 1.78	6.63 ± 0.16	0.40 ± 0.09	0.30 ± 0.07	1960 (2)
27	14.7 ± 0.22	11.9 ± 1.79	2.82 ± 0.15	0.60 ± 0.13	0.63 ± 0.14	1957 (2)
29	17.0 ± 0.25	9.07 ± 1.55	7.94 ± 0.17	0.15 ± 0.04	0.16 ± 0.04	1946 (2)
31	14.9 ± 0.22	11.6 ± 1.91	3.36 ± 0.17	0.26 ± 0.06	0.30 ± 0.07	1939 (2)
33	14.4 ± 0.21	9.44 ± 1.59	4.96 ± 0.17	0.18 ± 0.04	0.15 ± 0.03	1929 (3)
35	13.3 ± 0.20	8.00 ± 1.57	5.30 ± 0.20	0.14 ± 0.03	0.10 ± 0.02	1918 (3)
37	13.0 ± 0.19	10.5 ± 1.75	2.51 ± 0.17	0.13 ± 0.03	0.14 ± 0.03	1904 (4)
39	12.9 ± 0.19	10.9 ± 1.80	1.95 ± 0.17	0.11 ± 0.03	0.11 ± 0.03	1890 (5)
41	13.4 ± 0.20	12.7 ± 1.96	0.80 ± 0.16	0.18 ± 0.07	0.20 ± 0.08	1879 (8)
43	14.2 ± 0.21	11.8 ± 1.83	2.34 ± 0.16	-	-	-